BRNO UNIVERSITY OF TECHNOLOGY

VYSOKÉ UČENÍ TECHNICKÉ V BRNĚ

FACULTY OF MECHANICAL ENGINEERING

FAKULTA STROJNÍHO INŽENÝRSTVÍ

INSTITUTE OF PHYSICAL ENGINEERING

ÚSTAV FYZIKÁLNÍHO INŽENÝRSTVÍ

ANION-EXCHANGE ENABLED TUNING OF CAESIUM LEAD MIXED-HALIDE PEROVSKITES FOR HIGH-ENERGY RADIATION DETECTION

LADITELNOST CESIUM OLOVNATÝCH HALOGENIDOVÝCH PEROVSKITŮ UMOŽNĚNÁ VÝMĚNOU ANIONTŮ PRO DETEKCI VYSOKOENERGIOVÉHO ZÁŘENÍ

MASTER'S THESIS
DIPLOMOVÁ PRÁCE

AUTHOR　　　　　　　　　Bc. Radovan Matula
AUTOR PRÁCE

SUPERVISOR　　　　　　　Ing. Petr Dvořák, Ph.D.
VEDOUCÍ PRÁCE

BRNO 2024

Assignment Master's Thesis

Institut:	Institute of Physical Engineering
Student:	**Bc. Radovan Matula**
Degree programm:	Physical Engineering and Nanotechnology
Branch:	no specialisation
Supervisor:	**Ing. Petr Dvořák, Ph.D.**
Academic year:	2023/24

As provided for by the Act No. 111/98 Coll. on higher education institutions and the BUT Study and Examination Regulations, the director of the Institute hereby assigns the following topic of Master's Thesis:

Anion–exchange enabled tuning of caesium lead mixed–halide perovskites for high–energy radiation detection

Brief Description:

Lead halide perovskites (LHPs) have revolutionised the field of optoelectronics. LHPs' unique optoelectronic properties such as highly tunable bandgap, high stopping power, or large absorption cross–section, make them perfect candidates to be the semiconductor basis of a solid–state high–energy radiation detector. Varying the composition of LHPs furthermore leads to effective tuning of the aforementioned properties highlighting the already high significance and versatility. However, the anion–exchange enabled tuning is hindered by a questionable chemical stability of the resulting compounds. While lead halide perovskites show immense promise for high–energy radiation detection, addressing the issue of chemical stability is paramount to fully harness their potential.

Master's Thesis goals:

1. Research on the properties of lead halide perovskites for high–energy radiation detection.
2. Briefly describe the appropriate theoretical and simulation tools to describe the molecular dynamics of anion exchange in LHP.
3. Using theoretical and simulation tools, investigate the chemical stability and configuration of different halide concentrations in LHP.
4. Subject stable compounds to electronic structure calculations and estimate their suitability for high–energy radiation detection.
5. Compare your conclusions with available literature or experimental results and discuss the effectiveness of LHP detectors compared to conventional high–energy radiation detectors used today.

Recommended bibliography:

AKKERMAN, Quinten A., Gabriele RAINÒ, Maksym V. KOVALENKO a Liberato MANNA, 2018. Genesis, challenges and opportunities for colloidal lead halide perovskite nanocrystals. Nature Materials. 17(5), 394-405. ISSN 1476-1122. Dostupné z: doi:10.1038/s41563-018-0018-4

AKKERMAN, Quinten A., Valerio D'INNOCENZO, Sara ACCORNERO, Alice SCARPELLINI, Annamaria PETROZZA, Mirko PRATO a Liberato MANNA, 2015. Tuning the Optical Properties of Cesium Lead Halide Perovskite Nanocrystals by Anion Exchange Reactions. Journal of the American Chemical Society [online]. 2015-08-19, 137(32), 10276-10281 [cit. 2023-09-20]. ISSN 0002-7863. Dostupné z: doi:10.1021/jacs.5b05602

Deadline for submission Master's Thesis is given by the Schedule of the Academic year 2023/24

In Brno,

L. S.

prof. RNDr. Tomáš Šikola, CSc.	doc. Ing. Jiří Hlinka, Ph.D.
Director of the Institute	FME dean

Abstract

Lead halide perovskites (LHPs) with their unprecedented functional qualities which are only enhanced by the simple band gap tuning, have taken the world of semiconductors by storm. The process of anion exchange, possible even post-synthesis, allows for band gap tuning of LHPs, resulting in lead mixed-halide perovskites (LMHPs), thus expanding their potential for applications, notably in tuneable detectors. The widespread adoption of LMHPs is, however, hindered by their chemical instability, which leads to halide segregation in the material, seriously inhibiting reliable operation of any LMHP-based device. Understanding the kinetics of the halide segregation over extended periods remains a challenge, motivating the use of theoretical simulations like Monte Carlo (MC) methods. Yet, MC simulations rely on well-defined potential energy surfaces (PES), typically derived from computationally intensive density functional theory (DFT) calculations. In this thesis, we propose a novel approach for constructing well-defined PES from high-fidelity DFT data with fraction of the computational load. Utilizing activation-relaxation technique noveau (ARTn) motivated searches for transition points in the PES combined with state-of-the-art machine learning approaches, we aim to to significantly reduce computational costs. Additionally, employing classical theory, we assess the detection capabilities of selected LMHPs.

Abstrakt

Olovnato-halogenidové perovskity (OHP) se svými bezprecedentními funkčními vlastnostmi, které umocňuje jednoduché ladění zakázaného pásma, vzaly svět polovodičů útokem. Proces aniontové výměny, možný i po syntéze, umožňuje ladění zakázaného pásu OHP, což vede k olovnato-mix-halogenidovým perovskitům (OMHP), čímž se rozšiřuje jejich potenciál pro aplikace, zejména v oblasti laditelných detektorů. Širokému přijetí LMHP však brání jejich chemická nestabilita, která vede k segregaci halogenidů v materiálu, což zásadně omezuje spolehlivý provoz zařízení na bázi OMHP. Pochopení kinetiky segregace halogenidu přes delší časové intervaly zůstává výzvou, nabízi se tak použití teoretických simulací, jako jsou metody Monte Carlo (MC). Avšak MC simulace spoléhají na dobře definované povrchy potenciální energie (PPE), typicky odvozené z výpočetně náročných výpočtů teorie funkcionálu hustoty (DFT). V této práci navrhujeme nový přístup pro konstrukci dobře definovaných PPE z vysoce přesných DFT dat se zlomkem výpočetního zatížení. Využitím activation-relaxation technique noveau (ARTn) pro motivaci hledání přechodových bodů v PPE v kombinaci s nejmodernějšími přístupy strojového učení se snažíme výrazně snížit výpočetní náklady. Navíc s využitím klasické teorie hodnotíme detekční schopnosti vybraných OMHP.

Keywords
lead halide perovskites, advanced nanomaterials, tunability, machine-learning, density functional theory

Klíčová slova
olovnato-halogenidové perovskity, pokročilé nanomateriály, laditelnost, strojové učení, teorie funkcionálu hustoty

I hereby declare I have written this master thesis under the guidance of my thesis supervisor and that I have not used any sources other than those listed in the bibliography and identified as references.

Bc. Radovan Matula

Acknowledgement

Bc. Radovan Matula

One must imagine Sisyphus happy.

—Albert Camus [1]

Contents

Introduction

It has been fifteen years since Kojima et al. published their breakthrough paper, in which they first introduced the notion of lead halide perovskites (LHPs) being as visible light sensitizers for photovoltaic cells. Since then LHPs have seen a boom as many new functional properties and subsequent new applications were discovered. LHPs are a group of semiconductors known by their universal formula ABX_3, where A is in our case a cation of Cs, B is Pb and X = Cl, Br or I. Through the means of anion exchange, they allow for relatively simple band gap tuning. Their singular functional properties – highly tunable band gap, bright and narrow photoluminescence across the visible spectrum, high stopping power, unprecedented quantum yields – and cheap and easy production from chemical solutions, lend LHPs to many applications.

To exploit LHPs' capabilities to their fullest extent halide mixing has become the norm, resulting in use of lead mixed-halide perovksites (LMHPs), most often with composition $APbBr_{3-x}I_x$. LMHPs combining of iodine (I) and bromide (Br) are one of the most attractive candidates as varying the ratio of Br/I makes materials with band gaps suitable for high-efficiency tandem cells. Furthermore, in recent years, a technique utilizing organic ligands to transfer halides into an existing LHP structure has been introduced. Thus introducing the possibility of post-synthesis tuning, and opening the doors for applications such as tuneable detectors.

LMHPs are held back from mainstream use in solar cells due to their instability. When put under usual solar cell conditions, continuous wave illumination and applied electric field, they suffer reversible halide segregation into separate halide domains, which directly affects the cell's power conversion efficiency. Nonetheless, recent research suggests the presence of a metal ion on the A position further improves the stability of the compound and prevents significant phase segregation in the crystal, therefore in this research we will focus specifically on caesium LMHPs.

Though the chemistry of the mixing and demixing of the halides in the LMHP compound has been well studied, the physics governing the segregation and the creation of single-halide domains is not well understood. To remedy this blind spot a rigorous theoretical analysis of the process by means of ab-initio simulations is required. In order to simulate the evolution of such complex system with the Monte Carlo (MC) technique over a considerable period, we require the potential energy surface (PES) to be accurate, as the energy values appear in the exponential term of the probability of transition calculated during the MC simulation. DFT offers the necessary accuracy, however the method's poor scalability limits its use to small systems and short simulation times.

One viable alternative is the use of machine learning interatomic potentials (MLIPs) to describe the PES. This method doesn't necessitate the sacrifice of the high accuracy provided by ab-initio methods the same way a classical potential would, while maintaining favourable computational efficiency. Neural network interatomic potentials (NN-IP)

were previously limited in their applicability by the need for large ab-initio training set. Allegro is an equivariant deep learning variant of a message passing neural network (MPNN), which retains the accuracy of the previous NN-IPs but improves on them by introducing strict locality, thus enabling scaling to large systems. Thus the problem turns into search for the right data set for training of the high-fidelity PES.

In this thesis, we introduce a novel approach to PES exploration. Thusly constructed PES can be further used in MC simulations, the results of which we hope will open an easier path to the study of the halide segregation in the LMHPs and the discovery of more stable LMHPs for application in high-energy radiation detection.

1. Lead Mixed-Halide Perovskites

After spending almost a century being overlooked, lead halide perovskites (LHPs) have entered the scientific consciousness and garnered considerable attention in circa 2009 when Kojima et al. have decided to use the then fairly unknown material as a thin-film light absorber layer in their solar cell [2]. LHPs are named after the mineral Perovskite, with which they share its general structure, the basis of which are corner-sharing PbX_6 octahedra forming a cubic lattice. The cavities created between the octahedra, the A-sites, are filled by one or a combination of three large cations – Cs^+, $CH_3NH_3^+$ (MA^+), $CH(NH_2)_2^+$ (FA^+) – resulting in the general LHP formula $APbX_3$, see Figure 1.1.

LHP's eponymous structure that is the origin of their unique optical and functional properties, such as highly tunable bandgap, bright and narrow photoluminescence across the visible spectrum, high stopping power, unprecedented quantum yields, and cheap and easy production from chemical solutions, which have helped them generate notable attention in the scientific community over the last decade [2–11]. All these qualitites lend LHPs to many applications, those include solar cells [12], LEDs [13], light absorbers [14], optically pumped lasers [15], or high-energy radiation detection [16].

Cs   Pb   X = Cl, Br, I
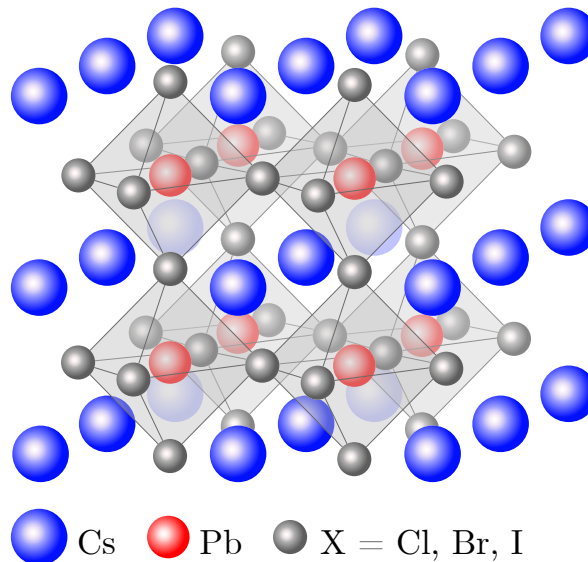
Figure 1.1: The structure of LHPs is formed by PbX_6 octahedra arranged in a cubic lattice, with heavy metal cations, in this case Cs^+, filling the cavities created by stacking of the octahedra.

One of the most common method of LHP production is the hot injection method. The key to the method lies in mixing the correct ratio of lead-halide and caesium precursor, alongside the addition of oleic acid (OA) or oleylamine (OLA). OA and OLA play a dual role, triggering the nucleation and growth of the nanocrystals (NCs), while

also aiding in the surface passivation of said NCs [17]. The temperature and quenching time determine the kinetics of the growth, thus deciding the quality of the prepared NCs. For example $CsPbBr_3$ nanocubes are converted to non-emitting tetragonal Cs_2PbBr_5 nanosheets at very high temperatures as described by Dutta et al. [18].

LHPs' single most interesting quality is their highly tuneable band gap. Tuning involves simply adjusting the ratio of the lead-halide precursors. The most common combination being $APbBr_{3-x}I_x$. LHPs combining iodine and bromine are one of the most attractive candidates. Increasing the Br:I ratio enables the tuning of the band gap from 2.43 eV to 1.48 eV with a continuous red shift [19], and creates materials with band gaps suitable for high-efficiency tandem cells [20], see Figure 1.2a.
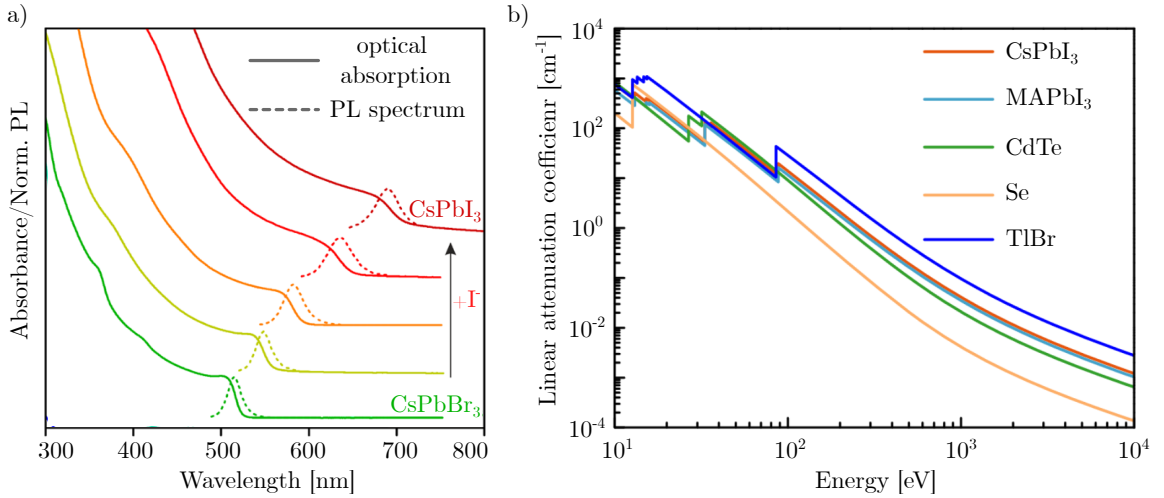

Figure 1.2: a) The change in optical absorption (solid lines) and PL spectra (dashed lines) of $CsPbBr_3$ NCs as PbI_2 is added as a source of exchanging halide anions. Image adapted from [21]. b) Linear attenuation coefficient against energy for several common semiconductor materials used in ionizing radiation detectors compared to LHPs $CsPbI_3$ and $MAPbI_3$, showing the LHPs to outperform most of the standardly used materials, especially at high energies. Image adapted from [22].

Stoumpos et al. [23] have first considered a $CsPbBr_3$ perovskite for use in X- and γ-ray detection in 2013 and found it to be highly promising. The hunger for newer, cheaper, and more efficient materials has led to LHPs being considered for use across the entire spectrum in radiation detection. For a material to be considered suitably efficient for use in solid-state detection devices it has to simultaneously exhibit certain characteristics:

- High average atomic number Z, which is related to the photoelectric absorption cross-section of a detector.

- Large resistivity, to ensure the lowest noise possible.

- High mobility-lifetime product $\mu\tau$, larger product means a lower probability of carriers being recombined (the highest product is in single crystalline semiconductors).

LHPs can meet all the criteria, while being cheap and easy to produce and having high tolerance to radiation damage [16, 24, 25].

Table 1.1 summarizes the X-ray detection performance of materials commonly used in current detectors, along with currently emerging new candidates including three LHPs. Si, is due to its low stopping to X-rays, delegated mainly to portable detectors [26]. The most commonly used material in direct conversion, α-Se, has stopping power 10 times greater than that of Si, however its production is expensive [27, 28]. HgI_2 and $Cd_{1-x}Zn_xTe$ (CZT, x<20%) both show great promise, with good sensitivities as shown in Table 1.1, however both materials have their limitations. HgI_2 suffers large leakage current, while CZT is difficult to integrate within read-out circuitry as it requires high temperature for high-quality crystal growth [22]. The current state-of-the-art CsI(Tl)-based detectors perform the best out of the traditional materials [29, 30].

The LHPs show themselves to be at least comparable to the traditional materials, while outperforming their predecessors in some metrics, as seen in Table 1.1. $MAPbBr_3$ appears to be the best candidate of the ones shown, however the poor stability of LHPs with organic A-position molecule detract from its merits. The third LHP presented, $CsPbBr_3$, also yields better results when compared to the traditional materials, while exhibiting greater chemical stability to $MAPbBr_3$ [31].

Table 1.1: Comparison of detection capabilities of classically used materials and LHPs

	Atomic number	Applied electric field [$V\,\mu m^{-1}$]	$\mu\tau$ product [$cm^2\,V^{-1}$]	Sensitivity [$\mu C\,Gy_{air}^{-1}\,cm^{-2}$]	Spatial resolution [$lp\,mm^{-1}$]	Lowest detectable dose rate [$\mu Gy_{air}\,s^{-1}$]	Refs
Si	14	0.5	>1	8	4.5	<8300	[26, 32]
α-Se	34	10	10^{-7}	20	-15	5.5	[28, 33]
HgI_2	53, 80	10	10^{-4}	1600	3.93	10	[34]
CZT	48, 52	0.1-1	0.01	318	10	50	[35, 36]
CsI(Tl)	53, 55, 81	–	–	5370	10	0.18	[29, 30]
$MAPbI_3$	53, 82	0.24	0.010	1.1×10^4	3	<5000	[37]
$MAPbBr_3$	35, 82	0.05	0.012	2.1×10^4	10	0.039	[38, 39]
$CsPbBr_3$	35, 82	0.005	0.013	5.6×10^4	9.8	0.215	[40, 41]

Zhang et al. [42] implemented anion exchange to improve the trap density and resistivity of $CsPbBr_3$ SCs and have discovered that the $CsPbBr_{2.9}I_{0.1}$ perovskite exhibits record sensitivity of $6.3 \times 10^4 \mu C\,Gy^{-1}\,cm^{-2}$ and a low detection limit $117\,nGy\,s^{-1}$ for 120 keV hard X-rays along with stable detection capabilities in an ambient environment for over 30 days.

The capability to fine-tune the band gap after synthesis would provide additional motivation for employing LHPs in scintillator or high-resolution display applications. Thanks to their structure and high defect tolerance LHPs allow for such change in structure and composition via the means of anion exchange [43]. The nanostructures best suited for this process are colloidal NCs due to their high volume-to-surface ratio and short diffusion path lengths [21]. The anion exchange is conducted by mixing the LHP NCs with a halide precursor, e.g., tetrabutyl halides (TBA-X), octadeculammonium halides (ODA-X), oleylammonium halides (OLAM-X), see Figure 1.3a. For the highly soluble precursors (OLAM-X and TBA-X), the reaction takes no more than a few seconds. The exchange can be monitored by observing the changes in the optical absorption and PL spectra [44], see Figure 1.3b and c.

One big hurdle holding back LHPs from mainstream applicability is their chemical instability. LHPs' good solubility in polar solvents, as useful as it is for easy thin film fabrication, compromises structural integrity of the NCs over longer periods of time. Caesium LHPs experience the lowest solubility, however even if low, this feature still poses a threat to structural integrity of the NCs [45].

Despite being stable against oxidation, LHPs' long-term stability in the combined
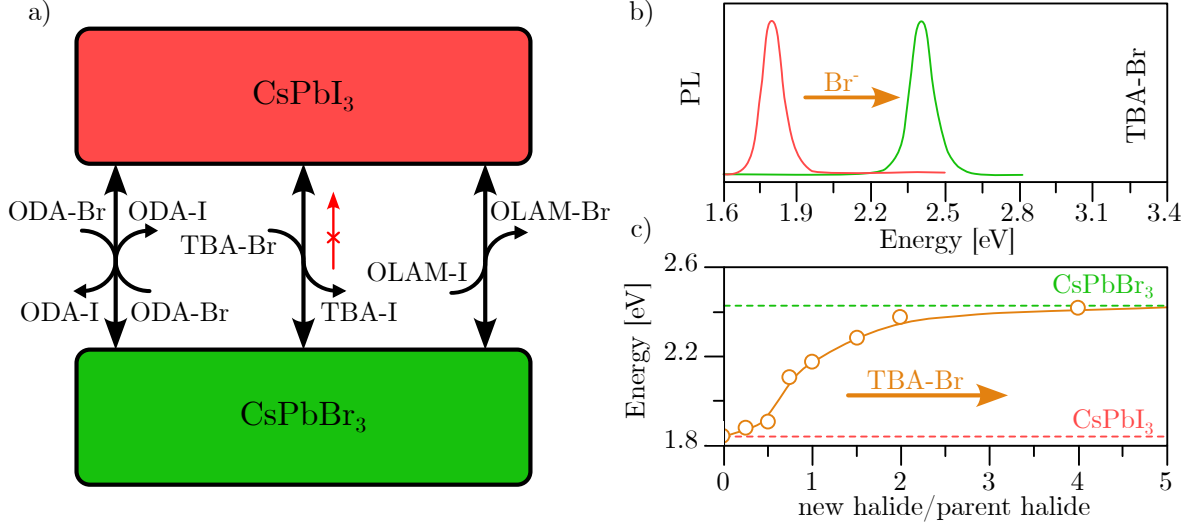
Figure 1.3: a) Schematic showing achievable anion exchange reaction for three precursors (ODA, TBA, OLAM) tested in [44]. b) Change in PL of the LHP NC after adding TBA-Br. c) PL calibration curve for anion exchange starting from pure $CsPbI_3$, using TBA-Br. The curve is given as a function of the ration of molar masses of the added and original halide. Images adapted from [44].

presence of light, moisture, and oxygen is questionable [46]. There are several proposed routes to take in order to improve the LHPs stability to environmental factors. The change in composition is one of the studied possible advancements in this area. Caesium once again proves to be beneficial as the presence of Cs in the lattice improves stability of the LHP against humid environment and irradiation compared to fully organic $MAPbX_3$ or $FAPbX_3$ [47–49]. One of the most well tested techniques for improving the lifetime of solar cell materials is encapsulation. This approach encloses the LHP NCs into SiO_2 which results in ceramic-like stability for the NCs, while retaining 100% of the original PL intensity [50].

Furthermore, the use of lead mixed-halide perovskites (LMHPs) is further hindered by the halide segregation occurring when the material is put under usual solar cell conditions, i.e., continuous wave illumination and applied electric field. While the segregation is reversible it does negatively impact the power conversion efficiency of the solar cell [51].

Though the chemistry of the mixing and demixing of the halides in the LMHP compound has been well studied [19], the physics governing the segregation and the creation of single-halide domains is not well understood [3, 52]. To remedy this blind spot a rigorous theoretical analysis of the process by means of ab-initio simulations is required.

In this thesis, we aim to exploit the singular properties of LMHPs to design a material to serve as a basis for a cheap and quality solid-state detector, specifically focusing on the area of hard X-rays (>10 keV). Through anion exchange we aim to passively tune the material to achieve high stopping power and a large X-ray absorption cross-section.

2.   Detection of High-energy Radiation

Ever since their discoveries both X- and γ-rays have become an integral part of various fields of study and with that came the need for efficient and large-area detection. Contemporary X-ray detectors can be classified into two categories by their approach to detection, direct and indirect, both of which contain semiconducting material which is responsible for absorption of the high-energy photons and their subsequent conversion into either a visible-spectrum photon or an electron [24]. However, the materials commonly used (Si, α-Se, CsI(Tl)) are lacking severely in several important areas, e.g., low X-ray absorption cross-section (linear cross-section coefficient to 50 keV of CsPbBr$_3$ quantum dots is 35 times larger than that of Si [53]), material instability, limited spatial resolution, or difficult tuning of their radioluminescence across the visible spectrum [25]. This makes the detectors expensive and ineffective at best but also a potential health risk in the case of use in the medical field where one cannot afford higher doses of radiation needed to compensate for low absorption.

On the electromagnetic spectrum the region of high-energy, or ionizing, radiation starts after ultraviolet radiation bellow $\lambda \sim 10^{-10}$ m (also $f \sim 10^{18}$ Hz), which according to $E = hc/\lambda$ corresponds to energies higher than (5–10) eV. In nature, ionizing radiation is created by the means of radioactive decay, this includes α, β, or γ-rays. Among artificial sources belong particle accelerators, nuclear fission, or X-ray tubes, which generate X-rays. The classification of "high-energy" stems from the shared characteristic of these radiation types: they possess sufficient energy to ionize the atoms they encounter. While this property is immensely beneficial in sectors like nuclear power, industrial manufacturing, and medicine, it also poses significant risks to living organisms. Consequently, there is a pressing demand for effective and reliable detection methods for such radiation.

Solid-state, or semiconductor, detectors (Figure 2.1a) use semiconductors in their architecture to absorb the incoming X-rays, and convert their energy into detectable quantities. Direct detectors convert the X-rays into an electron-hole pair and electric charge, that is proportional to the absorbed X-ray. The charge is captured by electric field to ensure maximal spatial resolution, by keeping the charge localised. The charge is then detected by a read-out component of the detector, and further analysed [54, 55].

Indirect, or scintillator, detectors (Figure 2.1b) consist of a layer of scintillating material and an electronic light sensor, e.g., a photodiode, silicone photomultiplier, or a photo multiplier tube (PMT). Scintillator is a device capable of absorbing the energy of an incoming particle and re-emitting it in the form of light in the visible spectrum. The visible-spectrum photon, provided it has energy greater than the band gap of the scintillating semiconductor, excites an electron from the valence band into the conduction band, creating an electron-hole pair in the process. Applying bias pulls electrons and holes in opposite directions, resulting in photocurrent. The photoelectrons

are then further multiplied, which results in a detectable electrical pulse [54, 55].

Gas detectors measure the dose rate of the X-rays absorbed by the gas. As the gas absorbs the X-rays it becomes ionized, i.e., creating pairs of ions and free electrons, under applied electric field each member of the pair is pulled in the opposite direction, generating detectable current [56].
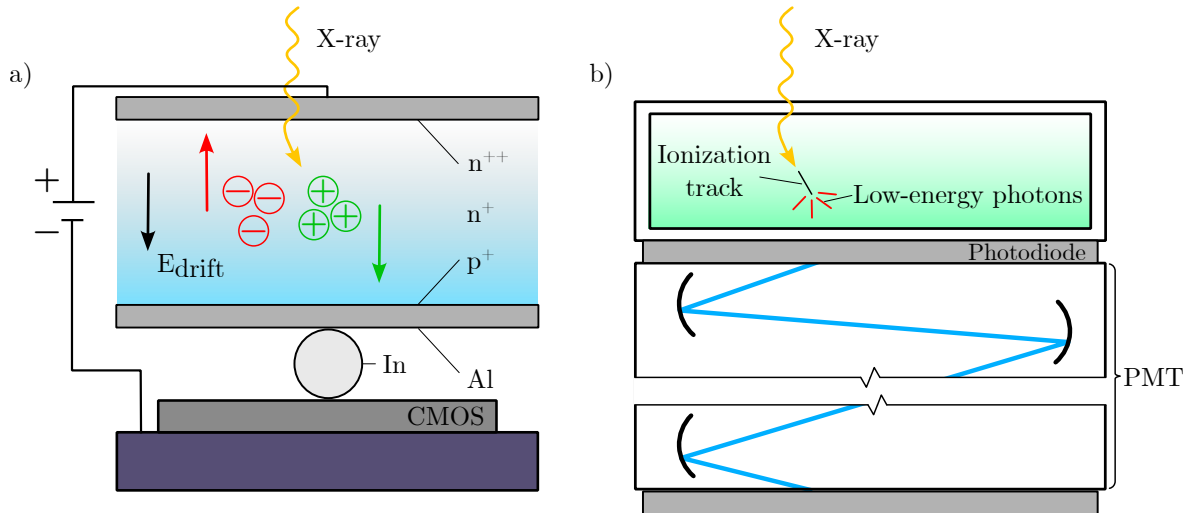

Figure 2.1: a) Semiconductor (direct) detector. Image adapted from [57]. b) Scintillator (indirect) detector. Image adapted from [58].

High-energy radiation detectors are needed in every field which deals with high energy radiation, therefore their applications are broad and varied. From medical diagnostics with radiography, mammography, or computed tomography (CT). CT also finds applications in industrial setting in material analysis, or defect inspection. To science, where detectors are a part of many common techniques, such as EDX spectroscopy, X-ray astronomy, XPS, or again CT. To even everyday life, in airport security, smoke detectors or Geiger counters, which both utilize gas detectors.

Material intended for use in semiconductor detectors need to exhibit efficient absorption over wide spectrum, high charge carrier mobility, long-term operational stability, and low-cost scale-up. Standardly used materials in commercial detectors, like Si or GaN require complex and costly equipment, along with process-intensive high-vacuum techniques. Meanwhile, a popular alternative capable of all the aforementioned features while being cheap to produce has recently emerged – lead halide perovskites (LHPs). LHPs have been considered for both direct and indirect detectors but are being held back by their subpar chemical stability. The goal of this thesis is not to design a detector, but merely to propose a material well-suited for the use in scintillator detectors, as that is the area where the use of LHPs is the most advanced.

3. Ab-initio Codes

This chapter serves as a non-exhaustive overview of ab-initio tools used in the creation and exploration of the *potential energy surface* (PES), needed for the Monte Carlo simulation of the halide segregation in lead mixed-halide perovskites.

3.1 Density Functional Theory

Density functional theory (DFT) serves as an alternative approach to quantum mechanics. It employs the Born-Oppenheimer approximation along with a number of others, to approximate the extremely complex many-body problems and provides a way to solve them in a satisfactory manner within finite and manageable time periods. DFT transforms the problem of solving the Schrödinger equation into the search for the ground state of a given quantum system, described by the Kohn-Sham equations (KSEs), which is achieved by minimizing the electron density functional [59, 60].

The self-consistent field (SCF) method, employs an iterative process to solve for a simpler approximation of the wave function. The algorithm of the SCF calculation is shown in Figure 3.1. The process starts with the initial guess of the electron density $\rho_i(\mathbf{r})$ from which effective potential $v_{\mathrm{eff},i}(\mathbf{r})$ is calculated. The KSEs are solved for the effective potential $v_{\mathrm{eff},i}$ resulting in new electron density $\rho_{i+1}(\mathbf{r})$. Total energy is calculated using the new electron density and the values are evaluated against a convergence threshold. Convergence is reached once the energy difference $\Delta E = E_i - E_{i-1}$ is lesser than the threshold. Should the convergence not be reached in the given iteration, the electron density ρ_{i+1} is plugged into the algorithm as the new input and the process is repeated. Once convergence is reached, the desired output is calculated. In this thesis, the DFT-SCF method is used for calculation of structure's energies and forces.

In this time and age, DFT has come to a point where it can reliably reproduce high-quality results over various methods and implementations. DFT has found its use in science, e.g., solid-state physics or quantum chemistry, as well as in metallurgy and pharmaceutical design; the number of papers regarding the use of DFT, published every year, is reaching over $15\,000$ and growing [62, 63].

The advantage of DFT's precision is however in certain cases outweighed by the computational cost of such calculations. The problem lays in DFT's poor scaling with system size, thus restricting its use to small-scale system and short simulation times [64].
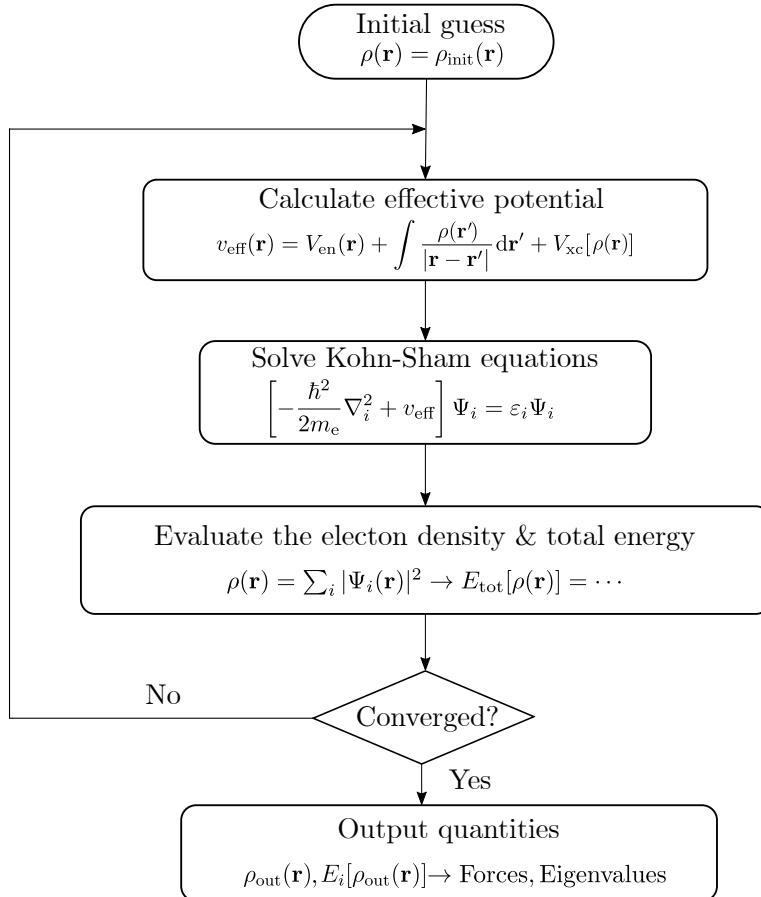
Figure 3.1: Diagram showing the process of an iterative DFT SCF calculation. It takes an initial guess of electron density ρ_{init} as input, this is then used to construct the effective potential v_{eff}. The v_{eff} then enters the Kohn-Sham equations, the result of which is a new electron density $\rho(\mathbf{r})$. Next total energy is calculated from the updated $\rho(\mathbf{r})$. Convergence is determined by comparing the energy difference between the total energies of the current and the previous step against a user-defined value. The process is repeated until convergence is reached. Energies and forces are calculated from the final electron density ρ_{out}. Adapted and edited from [61].

3.2 Molecular Dynamics

Molecular dynamics (MD) calculations is a method in computer simulations for analyzing the physical movement of particles in a particular system. The algorithm simulates the particle interactions over a fixed time period, thus giving a dynamic evolution of the many-body system. This is achieved by the means of exactly solving the classical equations of motion for the particles in question [65]. Usually, the particles creating the studied system are atoms.

Each i-th atom can be described by

$$\mathbf{F}_i = m_i \frac{\mathrm{d}^2 \mathbf{r}_i(t)}{\mathrm{d}t^2}, \tag{3.1}$$

where $\mathbf{r}_i = (x_i(t), y_i(t), z_i(t))$ is the position, m_i is the mass, and $\mathbf{F}_i$ is the force acting upon the i-th atom. To solve the equation 3.1, the required input parameters are the initial positions and velocities of the atoms, along with the forces acting upon

them.

Due to the complexity of the many-body problem the equation of motion needs to be discretized and solved numerically, e.g., using the Verlet algorithm [66]. The discrete time steps being no more than a few femtoseconds each. The time-dependent change in position is defined by $\mathbf{r}_i(t)$, while it's derivative $\mathbf{v}_i(t)$ determines the kinetic energy, and thus the instantaneous temperature, of the system. Each step of the algorithm consists of calculating the forces acting on i-th atom and moving the atoms, i.e., updating its position and velocity [67].

In using numerical integration to solve the Newton's equation of motion one wants to express the next position $\mathbf{r}_i(t + \Delta t)$ at time $t + \Delta t$ in terms of the previous position. The basic formula for the Verlet algorithm can be expressed from the Taylor expansion of $\mathbf{r}_i(t + \Delta t)$ [66]

$$\mathbf{r}_i(t + \Delta t) \cong 2\mathbf{r}_i(t) - \mathbf{r}_i(t - \Delta t) + \frac{\mathbf{F}_i(t)}{m_i}\Delta t^2. \tag{3.2}$$

MD Molecular Dynamics (MD) simulations offer insights into diverse processes, ranging from protein behavior to semiconductor research, providing atomic-scale resolution and precise temporal analysis from a classical perspective [68, 69]. This makes MD ideal for simulations on large ensembles and long time scale. None the less, simulations of this scale demand millions or even billions of computational steps, each involving potentially millions of interatomic interactions, resulting in substantial computational overhead. Nevertheless, advancements in computer hardware, such as GPUs, coupled with enhancements in MD software and algorithms, have significantly enhanced the accessibility and accuracy of MD simulations [70–73].

3.3 LAMMPS

Large-scale Atomic/Molecular Massively Parallel Simulator (LAMMPS) has become a popular and powerful computational engine for modeling interacting particles [74]. To achieve high computational efficiency LAMMPS implements neighbour lists to store information on particles within the cut-off distance. This feature allows LAMMPS to split the computational domain into sub-domains, where each of the parallel processors performs its part and the results from each one are then married to create the finished outcome. LAMMPS thus takes advantage of MD's scalability when the calculation is split into multiple parallel processes, as most tasks are easily parallelized, with each particle requiring only positional information about its neighbours during the force calculation [75]. Being open-source and mainly written in C++, LAMMPS allows for a relatively simple implementation of outside modules [76].

Numerical optimization is a cornerstone technique in condensed matter physics, frequently employed for various purposes. Typically, the target of optimization or minimization is the potential energy $E(\mathbf{r})$ with respect to the coordinates $\mathbf{r}$. The outcome of this optimization process provides equilibrium structures and energies at a temperature of 0K, such as those of defects. These configurations of minimum energy can subsequently serve as starting points for further computations, as will be shown in the following chapter [77].

Fast inertial relaxation engine (FIRE) is one of the most commonly used minimization algorithms. It relies solely on the gradient of energy, i.e., force, to arrive at

the minimum. Despite its simplicity in approach, it consistently delivers performance that rivals, and often surpasses, that of much more complex schemes [77]. To arrive at a minimum in the PES, FIRE follows the equation of motion given as

$$\dot{\mathbf{v}}(t) = \frac{1}{m}\mathbf{F}(t) - \gamma(t)|\mathbf{v}(t)|\left[\hat{\mathbf{v}}(t) - \hat{\mathbf{F}}(t)\right], \tag{3.3}$$

where m is mass of the particles in the system, their velocity is $\mathbf{v} = \dot{\mathbf{x}}$, force $\mathbf{F} = -\nabla E(\mathbf{r})$, and $\hat{\mathbf{v}}$ and $\hat{\mathbf{F}}$ denote unit vectors. The scalar function of time $\gamma(t)$ is optimized throughout the run of the algorithm. The goal of the algorithm thus is to descend in the direction 'steeper' than was the direction before a given point. This is done by the correct choice of the $\gamma(t)$ function. The value power is calculated as $P(t) = \mathbf{F}(t)\cdot\mathbf{v}(t)$ and if the result is negative, the algorithm halts its propagation and corrects itself once again by an appropriate choice of $\gamma(t)$.

The numerical side of the algorithm can be handled by any commonly used integrator, such as the Verlet algorithm (equation 3.2), which provides the propagation of the MD trajectories. Those are readjusted at each step by two velocity modifications: (1) the aforementioned uphill motion check, and (2) the combination of global velocity and updated force vector, given as: $\mathbf{v} \rightarrow (1-\alpha)\mathbf{v} + \alpha\hat{\mathbf{F}}|\mathbf{v}|$; with the parameter α and time step Δt, which are both of chosen adaptively at each step [77–79]. The diagram of the calculation is shown in Figure 3.2.
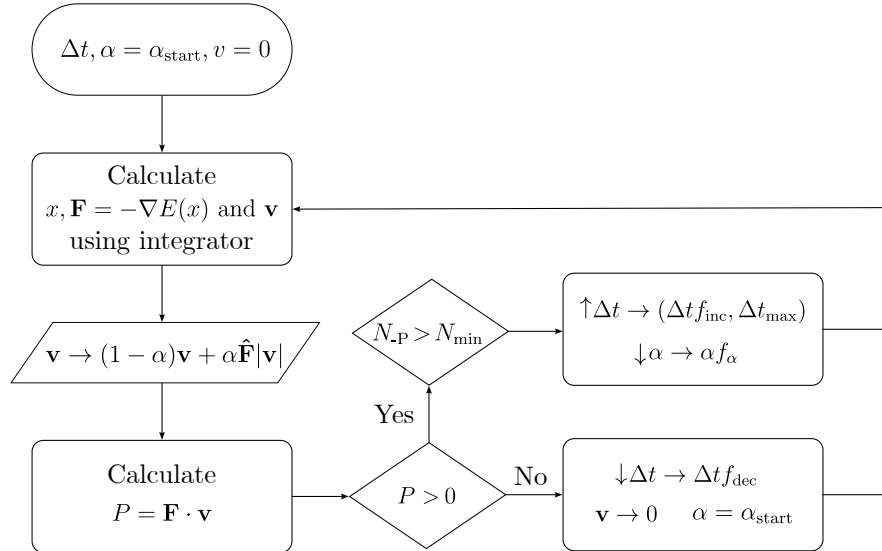
Figure 3.2: Schematic showing the process of FIRE arriving at a local minimum in the PES. The algorithm starts with given values for time step and the mixing factor α, with the velocity at zero. Next, FIRE uses a standard integrator, such as Verlet, to calculate the current position, velocity and forces. This is followed by convergence check. In case of not reaching convergence, the velocity is updated with a mix of global velocity and updated force, the mixing determined by the α factor. The power is calculated and evaluated. If it is negative the algorithm halts and resets the velocity and the mixing factor, and lowers the time step. If the value of power is positive and the number of steps since the last negative value is greater than a given threshold the time step is increased and α is decreased [78].

3.4 ARTn

Activation relaxation technique noveau (ARTn) is a highly efficient method intended to identify local transitions in a PES using only local information – energy and forces. The basis of the ARTn algorithm is formed by three steps (blue squares in Figure 3.3) which are repeated at each iteration until convergence is reached:

- finding the lowest curvature which corresponds to the lowest eigenvalue of the Hessian λ_m and its corresponding eigenvector $\mathbf{e}_\mathrm{m}$,

- uphill push, against the forces,

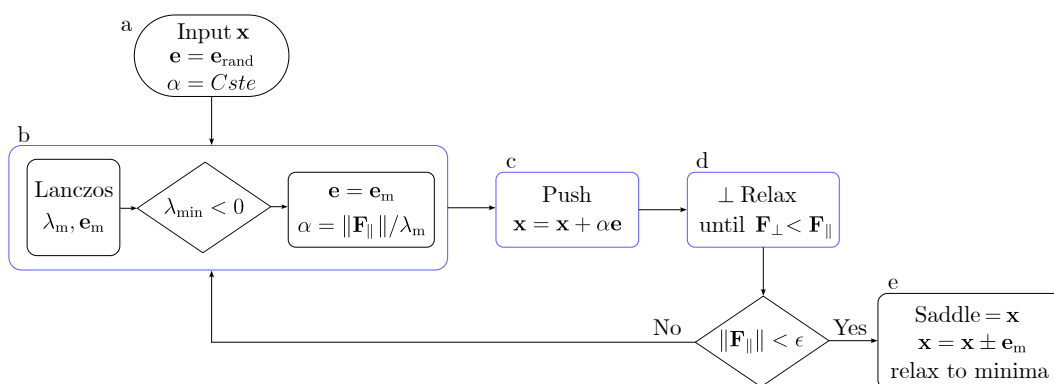- relaxation into the hyperplane perpendicular to the push.

Figure 3.3: Schematic showing the ARTn algorithm. The three main steps are denoted by a blue border. The algorithm starts with a given position and a random push. In practice several consecutive random pushed are performed in order to escape the minima basin. In the first step, ARTn uses the Lanczos algorithm to find the curvature and its corresponding eigenvector. These two values enter the second step, where they determine the size and direction of the ensuing push. The third step follows with relaxation in the direction perpendicular to the push. Eventually, the perpendicular relaxation arrives at the saddle point, thus having converged and the algorithm stop. The finding of a saddle point may be followed by a relaxation to a backward and forward minima. Adapted from [80].

The beginning of the first ARTn loop is preceded by an *initial uphill push*. This is done as it is otherwise impossible to obtain information about the sought after saddle point from the local minimum which is the starting structure for the algorithm. Random push $\mathbf{e}_\mathrm{rand}$ is generated from the local minimum to start the search for the saddle point, Figure 3.3a.

The Lanczos algorithm evaluates the Hessian and outputs the lowest eigenvalue λ_m and its corresponding eigenvector $\mathbf{e}_\mathrm{m}$ [81]. The goal is to determine whether the current position is above ($\lambda_\mathrm{m} < 0$), or still bellow ($\lambda_\mathrm{m} > 0$) the inflection hyperplane. While bellow the hyperplane, the system is repeatedly pushed in the random initial uphill direction, until escaping the concave region (minimum basin). For the sake of saving on computational costs the random push is performed several time before the first Lanczos evaluation. Once above the hyperplane, the push direction eigenvector is assigned value $\mathbf{e}_\mathrm{m}$, Figure 3.3b.

The uphill push once above the inflection hyperplane is updated after each ARTn loop as the eigenvector $\mathbf{e}_{\mathrm{m}}$ corresponding to the current lowest eigenvalue λ_{m} of the Hessian while $|\lambda_{\mathrm{m}}| > \lambda_{\mathrm{thr}}$, where λ_{thr} is a user set threshold for curvature convergence. The orientation of the push is set antiparallel to the force and the displacement norm for the push is set as

$$\mathrm{d}r = \min\left(\mathrm{size}_{\mathrm{max}}, \frac{\|\mathbf{F}_\|\|}{\max(|\lambda_{\mathrm{min}}|, 0.5)}\right), \tag{3.4}$$

where $\mathbf{F}_\|$ is the force component parallel to $\mathbf{e}_{\mathrm{min}}$ and $\mathrm{size}_{\mathrm{max}}$ is user defined threshold. This approach reduces the displacement as ARTn nears the saddle point and thus accelerates convergence, Figure 3.3c.

The saddle point on a given surface is the point where all the derivatives in the orthogonal directions are zero, but the point is not a local extreme, but rather saddle point is a maximum in one direction and a minimum in all the others [82]. The slope of the PES is by definition the force, and therefore the saddle point in the PES is denoted by $\mathbf{F}_\perp = 0$. To lower computational costs the orthogonal relaxation is stopped once $\mathbf{F}_\perp < \mathbf{F}_\|$, Figure 3.3d.

When the saddle point – point with $\mathbf{F}_\perp$ bellow a near-zero threshold and $\lambda_{\mathrm{m}} < 0$ – is reached, the system is given a push in the direction of the current $\mathbf{e}_{\mathrm{m}}$ and a standard minimization algorithm, e.g., FIRE, relaxes the system into a connected minimum. The connection is ensured by the choice of the push [80], Figure 3.3e.

The implementation of ARTn used further in this work is the plug-in ARTn (pARTn) developed by Poberznik et al [83]. pARTn works on the basis of hijacking the FIRE minimization algorithm. The hijacking is achieved by accessing the four quantities FIRE calculates at each step – $\mathbf{F}, \mathbf{v}, \alpha, \Delta t$ – and modifying them by imposing an external condition on the system. The hijacking scheme allows for an easy interfacing with LAMMPS and makes it possible to run ARTn within a LAMMPS calculation.

3.5   Machine-Learned Interatomic Potentials

The accuracy of a Potential Energy Surface (PES) is pivotal for ensuring the reliability of results in both MD and Monte Carlo (MC) simulations. Nonetheless, the computational expenses associated with DFT render it impractical for this purpose. Thus empirical potentials have become standard practice, despite the challenging process of constructing a reliable empirical potential. This difficulty stems from the necessity of fitting parameters for a guessed (albeit physically grounded) functional form of the interatomic potential, which can potentially yield qualitatively incorrect results. [84, 85].

The development of machine-learned interatomic potentials (MLIPs) was pioneered by Behler and Parrinello [85, 86]. This method utilizes ab-initio data as the input of the neural networks (NNs) at the center of the algorithm. NN based MLIPs combine the results of several element-specific NNs, each trained on one single-atom local environment of the studied structure, called symmetry functions. The output of the NNs are energy predictions which are summed up to from the total energy of the system, as is shown in Figure 3.4.

The problem with the first generation of MLIPs lay in the lack of predictive accuracy, as the networks were often unable to predict structures beyond the confines of the training data set [87]. Message-passing NNs (MPNNs) emerged as a remedy
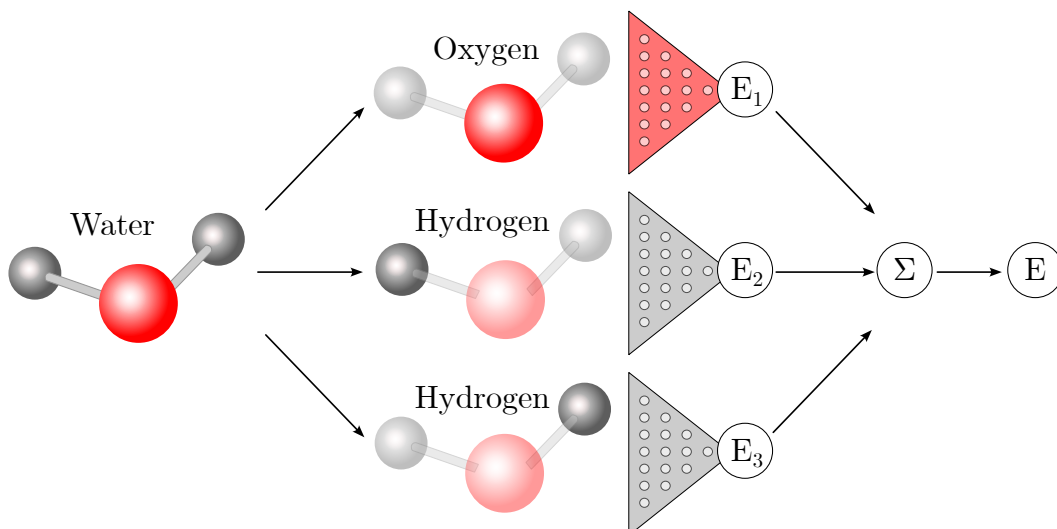
Figure 3.4: Schematic of the NN-based MLIPs. The studied system is split into element-specific single-atomic local environments. For each of those a dedicated NN produces an energy prediction. The energy predictions of each subpart are the summed up to the system's total energy. Adapted from [84].

to this issue, showcasing markedly improved accuracy, albeit at the expense of significant computational resources [88]. The transition from invariant MLIPs, which solely manipulate geometric invariants of a system, to equivariant MLIPs marked a significant leap forward in accuracy. Allegro is the first equivariant MLIP which was able to achieve the high accuracy of MPNNs while simultaneously offering scaling to large simulations, due to strict locality of its geometric representations [64, 88].

The task at hand thus becomes the correct choice of the DFT training set to achieve ab initio accuracy MLIP. The following chapter deals with the automatization of the process via a custom Python code.

4. Creation of the Machine-Learned Interatomic Potential

During my ERASMUS internship at the Institute Ruđer Bošković I have taken part in the development of a code for the iterative improvement of machine-learned interatomic potentials (MLIPs) via consecutive activation relaxation technique noveau (ARTn) runs. The latest version of the code entitled CAMUS can be found at [89].

The initial data set was generated from a set of LMHP structures of several lattice configurations by performing a molecular dynamics (MD) calculation using the VASP [90–92] code with the following parameters,

```
IBRION   =   0        # MD
NSW      =   200      # Number of steps
POTIM    =   2        # Duration of one step (in fs)
SMASS    =   -1       # Canonical ensemble
TEBEG    =   400      # K
MDALGO   =   0        # Verlet
```

which indicate an MD calculation performed for 200 steps, the duration of each being 2 fs, with continuous increase in the kinetic energy, beginning at the temperature of 400 K, using the Verlet algorithm, equation 3.2. This resulted in the starting data set of ≈ 1200 structures $\mathcal{M}_0$.

Further a subset of 200 structures was pseudo-randomly chosen out of $\mathcal{M}_0$, each of the structures had a caesium and a halide (either bromide or iodine) atom removed, to include the effect of vacancies in the MLIP. The resulting set is then split in a 80/20 ratio to create an *initial* and a *test* set, $\mathcal{M}_{\text{init}}$ and $\mathcal{M}_{\text{test}}$, respectively. The following paragraphs describe the process of creation of a high-fidelity MLIP for $CsPbBr_{3-x}I_x$ perovskite using the CAMUS code.

The initial training set $\mathcal{M}_{\text{init}}$ is clustered at the beginning of the process. The clustering happens at two levels. At the first level the structures are grouped based on chemical composition, thus preventing the unnecessary and computationally expensive descriptor-comparison of any two structures.

The second level clustering is executed withing the composition groups. Every structure is assigned an Atomic-Centered Symmetry Functions (ACSFs) descriptor. CAMUS implements the ACSF descriptors via the DScribe code [93, 94]. The ACSFs describe local environment around a central atom with the number of the considered neighbouring atoms determined by a cut-off radius r_{cut} [95]. The ACSF descriptor

$$\mathbf{D}_{\text{ACSF}} = (\mathbf{d}_1, \ldots, \mathbf{d}_{\text{n}}) \propto [(\mathbf{r}_{1,1}, \ldots, \mathbf{r}_{1,m}, \mathbf{Z}), \ldots, (\mathbf{r}_{m,1}, \ldots, \mathbf{r}_{m,m}, \mathbf{Z})], \qquad (4.1)$$

where $\mathbf{d}_i$ is a local atomic environment is created as an output of several two- and three-

body functions. They depend on the relation of the m neighbouring atoms belonging to each of the n atoms in the structure to that atom, and by their chemical species $\mathbf{Z}$.

With each structure of the set being issued a corresponding descriptors, the clustering algorithm proceeds to calculate the similarity metric between every pair of structures withing a composition group. The desired similarity value is calculated by building an *average kernel*, which for two structures is defined as

$$K(\text{A,B}) = \frac{1}{NM} \sum_{i,j} C_{i,j}(\text{A,B}),\tag{4.2}$$

where N,M are numbers of atoms of structures A and B, respectively. $C_{i,j}$ is the similarity between two local atomic environments and can be calculated by any pairwise metric, the Laplacian metric was chosen for the LMHP structures as it yielded the most intuitive similarity values.

Should the calculated pairwise similarity of any two structures exceed a user-set *similarity threshold* t_{sim}, these structures are considered 'similar' and thus flagged as *neigbours*. The algorithm finds a structure with the highest number of neighbours. This structure is the first *cluster center* and along with its list of neighbors is recorded as such and omitted from the next iteration. In each iteration a new cluster center and a corresponding neighbour or a list of neighbours are found, until all the structures left are not 'similar' to any other structure in the set. These 'dissimilar' structures are listed as *orphans*. The list of centers and orphans serve as the representatives of the whole $\mathcal{M}_{\text{init}}$. Figure 4.1 schematically shows the concept of clustering as is implemented in CAMUS.

● Cluster Center ○ Neigbour – – Cluster Border ● Represented Cluster ● Orphan
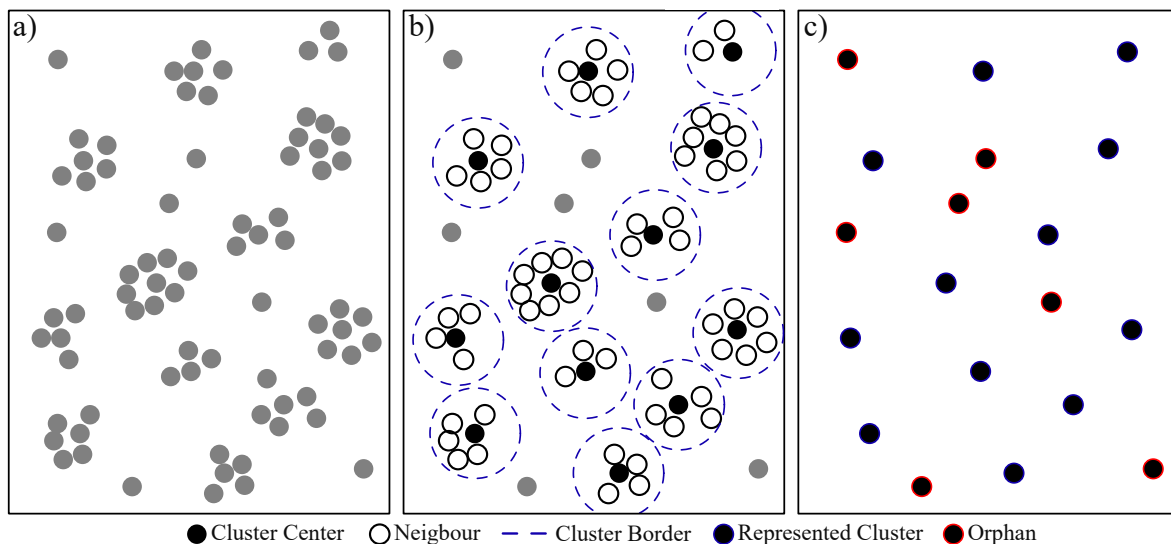
Figure 4.1: The descriptor-based similarity clustering finds a structure with the highest number of similar structures and chooses it as the first cluster center. The process is repeated until all clusters are identified. Should a structure be found not similar to any other it will be designated an *orphan*.

The clustering is performed for the optimization of the r_{cut} and t_{sim} parameters, and to prevent over-fitting of the network. For the r_{cut}, we determined the best value to be 7Å as a neighbourhood of this radius includes second neighbours. We clustered the set for $t_{\text{sim}} = (0.60, 0.70, 0.80, 0.90)$. For each of the created subsets of $\mathcal{M}_{\text{init}}$ we train three

networks and pick the best performing one. Each trained network is evaluated using Allegro's built-in `nequip-evaluate` method. This method uses the trained network to predict the energies of the structures form $\mathcal{M}_{\text{test}}$ and calculates the error between the predicted value and the 'correct' value included in $\mathcal{M}_{\text{test}}$. The errors calculated are mean absolute error (MAE), and root-mean square error (RMSE):

$$\text{MAE} = \frac{1}{N}\sum_{i=1}^{N}|e_i|, \qquad \text{RMSE} = \sqrt{\text{MAE}} = \sqrt{\frac{1}{N}\sum_{i=1}^{N}e_i}. \qquad (4.3)$$

In figure 4.2 we see the comparison of the networks within each triplet, as well as the comparison of networks for different cluster sizes. The network chosen is the one with the lowest error, `network-7-60` (corresponding to $r_{\text{cut}} = 7$ and $t_{\text{sim}} = 0.60$). The chosen network is deployed using `nequip-deploy`, which creates a potential file containing the PES fit compatible with LAMMPS.
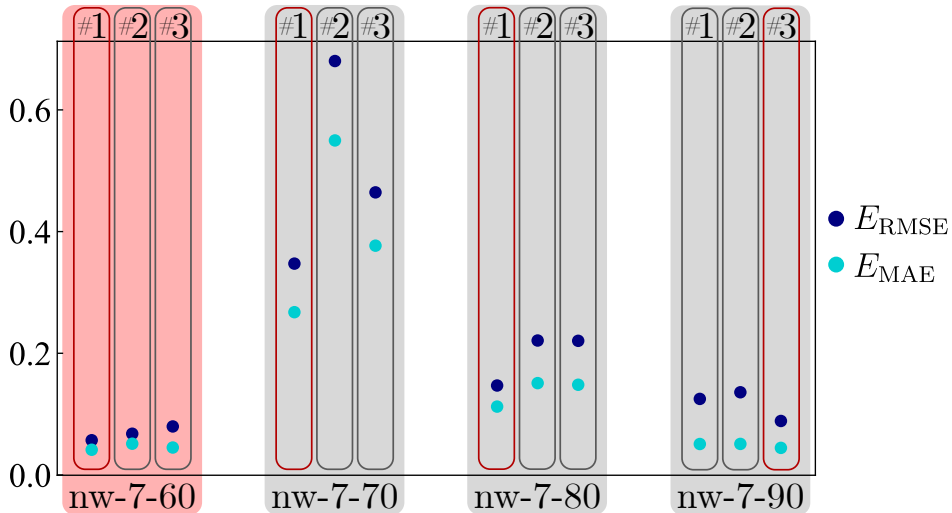

Figure 4.2: For each of the subset created by clustering for parameters $r_{\text{cut}} = 7\text{Å}$ and $t_{\text{sim}} = (0.60, 0.70, 0.80, 0.90)$, we trained three networks. From each trio the network with the lowest error is chosen (marked by red rectangle). The chosen ones are compared amongst each other and once again the one with the lowest errors is chosen. The chosen network is `network-7-60` as it has the lowest combination of errors.

The corresponding data set, sub set of $\mathcal{M}_{\text{init}}$, denoted as $\mathcal{M}_{\text{train},0}$, is minimized via LAMMPS using the current potential. The minimized structures will serve as the starting points of the *Sisyphus calculations*.

The Sisyphus algorithm serves as the essential building block of the CAMUS code. It performs a series of ARTn calculations with the purpose of defining transitions in the PES. The schematic of the Sisyphus algorithm is in Figure 4.3.

A Sisyphus calculation starts from a structure corresponding to a local minimum on the PES. The algorithm performs ARTn searches until it reaches a saddle point; the two companion minima of the saddle point are auditioned. At least one of the newly found minima must be 'close' to the starting one for the path to be considered *connected*. This is determined by the user-given delr$_{\text{thr}}$ parameter, which expresses the total displacement of the configuration from the initial configuration and is calculated by ARTn
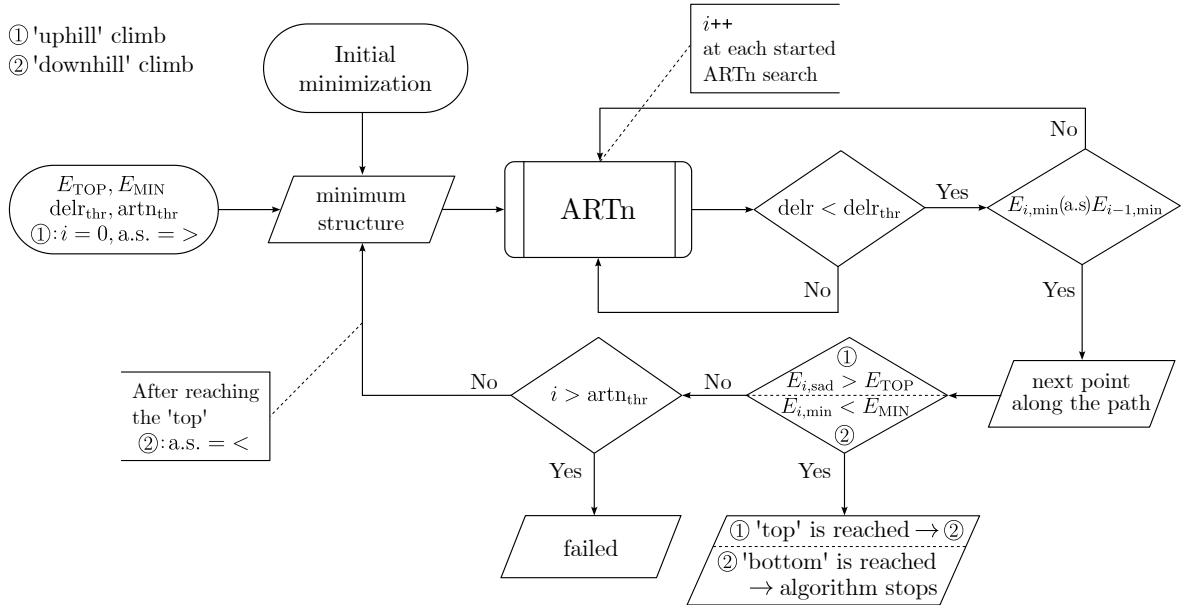
Figure 4.3: Flowchart describing the algorithm which results in Figure 4.6.

as a part of its output. Subsequently, the algorithm compares the delrs for both of the minima and determines which of the minima is further from the starting one. This minimum is auditioned as the next possible point along the path. It is accepted if it is energetically higher than the previous minimum, the acceptance sign is '>' during the *uphill climb*.

This process of performing ARTn searches and auditioning found saddle and minima points is repeated until the algorithm reaches a saddle point with energy greater than E_{TOP}, or runs out of the set number of ARTn searches. Once over E_{TOP} the algorithm stops, the energy of the final saddle point defines the energy height of the found transition.

At this point the acceptance sign changes to '<' and the *downhill climb* comences. The process is identical to the one described in the previous two paragraphs, except for the accepted minima now being energetically lower than the ones preceding them. The algorithm ends once a minimum with energy lower than E_{MIN} is found, or it runs out of the set number of ARTn searches. The result of a Sisyphus run is shown in Figure 4.6a.

The result, $\mathcal{M}^{(1)}_{train,0}$, is a large collection of new data points, many of which are possibly very similar to the starting set $\mathcal{M}_{train,0}$. Therefore we perform a second round of clustering, using the same parameters which were used in the original clustering ($r_{cut} = 7$ and $t_{sim} = 0.60$). The result of the clustering is $\mathcal{M}^{(2)}_{train,0}$, a set of representatives of $\mathcal{M}^{(1)}_{train,0}$.

Self-contained field (SCF) DFT calculations are performed on the structures contained in $\mathcal{M}^{(2)}_{train,0}$, to obtain the 'correct' energies and forces for the configurations generated by Sisyphus using the current MLIP. The energy evaluation is performed according to the algorithm shown in Figure 4.4.

The difference ΔE between the ML and DFT energies is evaluated against two user-set parameters E_{thr} and E_{max}. The former differentiates between well and poorly predicted structures, while the latter serves to filter out structures with extremely high energies, which are far beyond the well defined area of the MLIP, as these would then
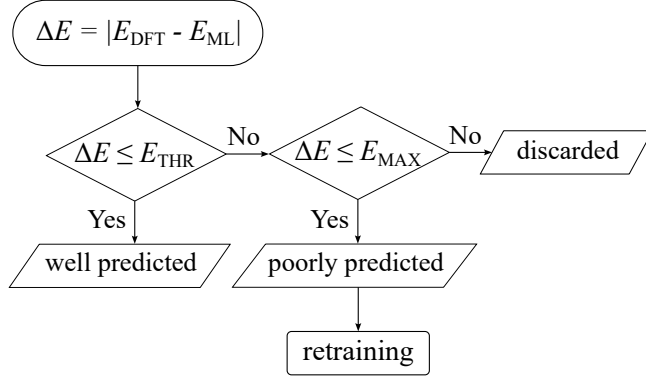
Figure 4.4: Schematic of the evaluation process. We evaluate the difference between the 'correct' energy from DFT calculation and the energy predicted by the MLIP.

skew the fitting of the network. The structures for which $\Delta E \in \langle E_{\text{thr}}, E_{\text{max}} \rangle$ become $\mathcal{M}^{(3)}_{\text{train},0}$. The training set for the next iteration of the network fitting via Allegro is given as

$$\mathcal{M}_{\text{train},1} = \mathcal{M}_{\text{train},0} + \mathcal{M}^{(3)}_{\text{train},0}.$$

The iterations that followed were executed in the same fashion. In total, three rounds of network training were performed. Figure 4.5 shows the improvement in accuracy over the four MLIPs. Each of the MLIPs were tested on an extended test set $\mathcal{M}_{\text{exttest}}$. The graph shows significant lowering of the MAE and RMSE (eqs 4.3) for the energies of $\mathcal{M}_{\text{exttest}}$ calculated with the MLIP of each iteration. The intended purpose of CAMUS is to create MLIPs for use in Monte Carlo simulations, which require well defined energy levels in the PES.
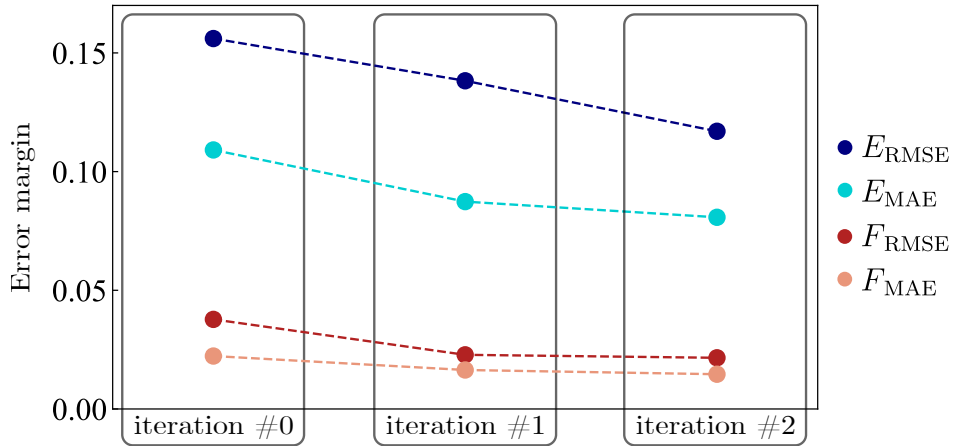
Figure 4.5: The initial network was improved over two iteration using the CAMUS process of adding relevant data points into the data set.

In this chapter we have shown that the method implemented in CAMUS is capable of significant improvement to the PES at a significantly reduced computational cost as we had to run DFT calculations only for a fraction of data points. Performing the MC simulations of the LMHPs halide segregation is beyond the scope of this thesis. Therefore we turn to published research to find a stable LMHP suitable for application in high-energy radiation detection. Zhang et al. introduce $CsPbBr_{2.9}I_{0.1}$ as the ideal

candidate due to its record sensitivity, high resistivity, and long term stability.
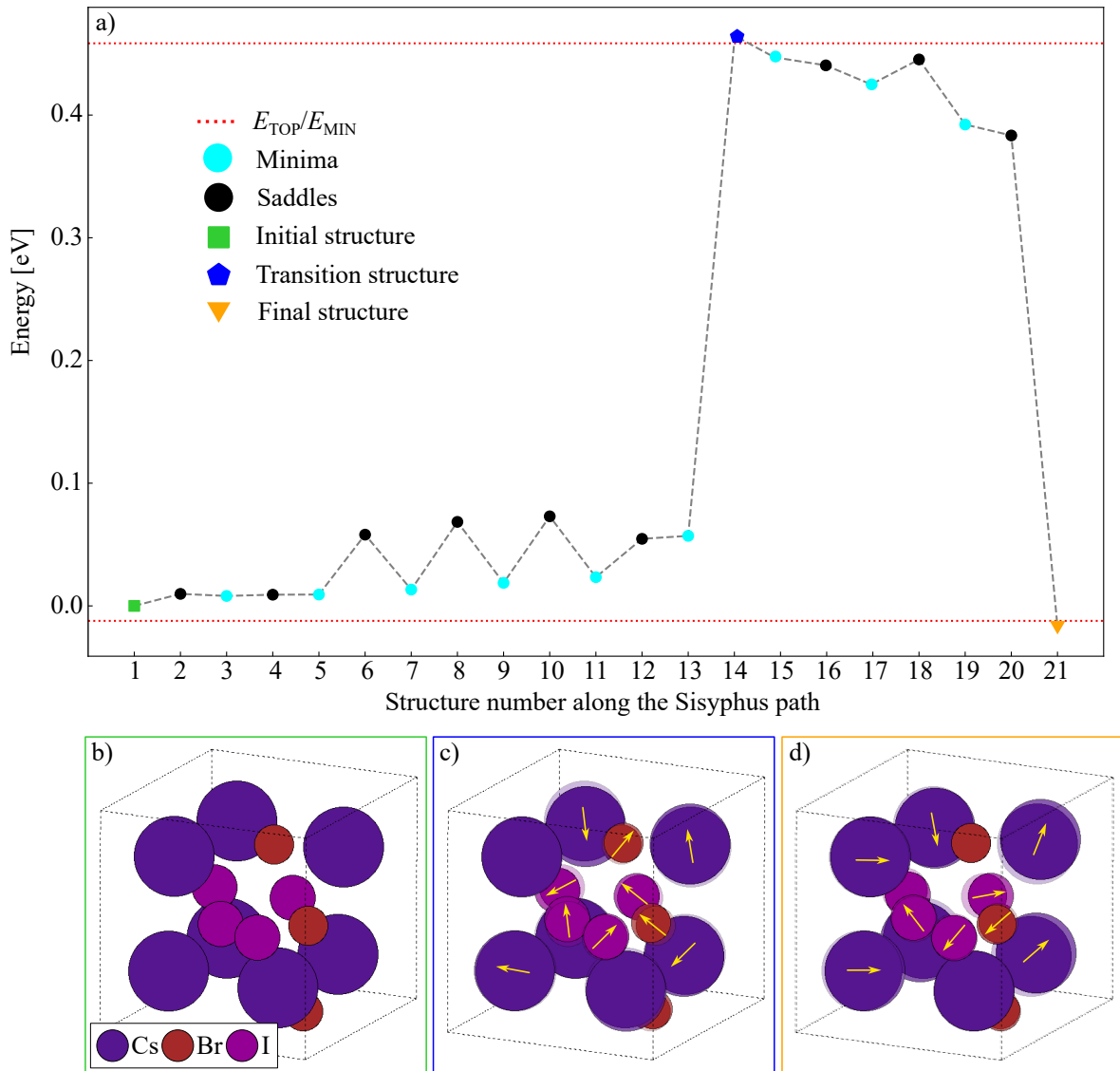
Figure 4.6: a) Plot of a successful Sisyphus run. The run starts from a minimized structure, by performing ARTn searches the algorithm finds new saddle points and its two companion minima, these minima are auditioned. New minimum is accepted if it is the further one from and it is energetically higher than the initial minimum. This process is repeated until a saddle point with energy greater than E_{TOP} – this is the transition point. The algorithm further descends into a minimum below E_{MIN}. Figures b)–d) show selected atoms from: b) the initial minimum structure, c) the structure corresponding to the transition point (on top overlaid b)), d) the final minimum (on top overlaid c)).

5. Calculation of Detection Capabilities

The ability of a material to reduce the impinging beam of radiation is expressed by the linear attenuation coefficient. Small attenuation coefficient would imply a relatively transparent material while large value would mean more opaque material, potentially ideal for application in detectors of such radiation. Attenuation coefficient of a volume is given as

$$\mu = -\frac{1}{\Phi_e}\frac{d\Phi_e}{dz},\tag{5.1}$$

where Φ_e is the radiant flux and z is the path length of the beam.

The energy carried by an X-ray is transferred into the target material by two different mechanisms – absorption and scattering. The processes occurring at the energy transfer are either ionization, in this case an electron is removed from the incident atom creating a positively charged ion, or excitation. During excitation the energy of the X-ray gets transferred to an electron in the incident atom's electron shells, temporarily increasing the electron's energy, thus moving it up into a higher energy level and the whole atom into a more energetic state.

There are three main processes that are important to take into consideration when an X-ray interacts with matter – the photoelectric effect, the Compton effect, and pair production (here we are specifically referring to the creation of electron-positron pairs). These three interactions are pictured in a schematic in Figure 5.1.

The photoelectric (PE) effect is the cause of the characteristic X-ray emission, but also it is a crucial secondary process in the interaction of X-rays with matter. For energies up to ~ 500 keV PE absorption is the dominant form of X-ray absorption, especially for atoms with higher atomic numbers. The impinging X-ray transfers its energy to an orbital electron. This photo-electron then leaves the atom at high speed [96]. The probability of PE occurring, and therefore contributing to the total interaction of the X-ray with the given matter, is given by its cross-section [97] as

$$\sigma_{PE} = \frac{16\sqrt{2}\pi}{3}r_e^2\alpha^4\frac{Z^5}{k^{3.5}},\tag{5.2}$$

where r_e is the classical electron radius, α is the fine structure constant, and $k = \frac{E_X}{E_e}$ is the ratio of the X-ray energy to the electrons rest mass energy $E_e = m_e c^2 \simeq 0.511$ MeV.

Compton scattering (CS), or incoherent scattering, is a process in which an X-ray imparts its energy to an atom's electron, ejecting him from its orbital, accompanied by a lower energy X-ray. The absorption due to CS is prevalent for energies between 100 keV–10 MeV, particularly for low atomic number elements. Generally, CS
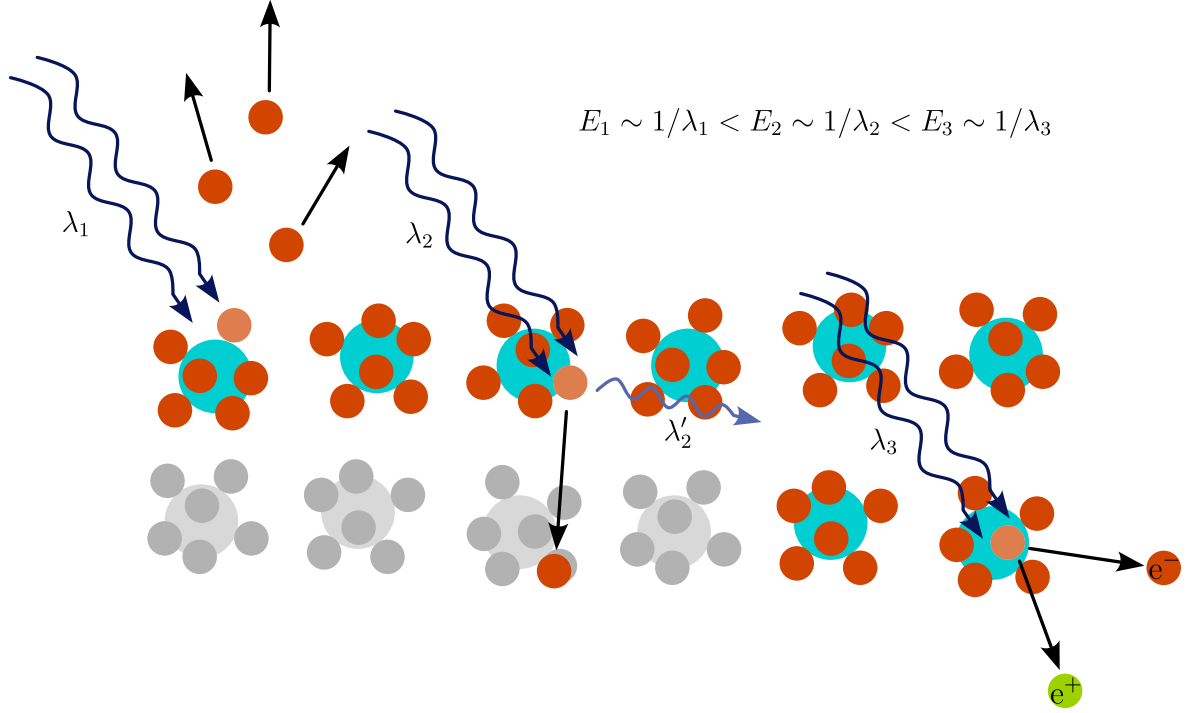
Figure 5.1: Three main processes governing the interaction of X-rays with matter: the photoelectric effect (λ_1), the Compton scattering (λ_2), and the pair production (λ_3).

is the overall background in X-ray diffraction measurements [98]. We use the Klein-Nishina [99, 100] formula to calculate the contribution of CS to the total absorption cross-section

$$\frac{\mathrm{d}\sigma_\mathrm{C}}{\mathrm{d}\Omega} = \frac{r_\mathrm{e}^2}{2}\left(\frac{E_\mathrm{X}'}{E_\mathrm{X}}\right)^2\left[\frac{E_\mathrm{X}'}{E_\mathrm{X}} + \frac{E_\mathrm{X}}{E_\mathrm{X}'} - \sin^2\theta\right], \tag{5.3}$$

where E_X and E_X' are the initial and final photon energy, respectively, and θ is the scattering angle. The ratio of initial and final photon energy can be expressed as

$$\frac{E_\mathrm{X}'}{E_\mathrm{X}} = \frac{\lambda}{\lambda'} = \frac{1}{1 + k(1 - \cos(\theta))}. \tag{5.4}$$

Integrating $\frac{\mathrm{d}\sigma_\mathrm{C}}{\mathrm{d}\Omega}$ over all solid angles yields the total Compton contribution

$$\sigma_\mathrm{C} = \int\limits_0^{2\pi}\int\limits_0^{\pi} \frac{\mathrm{d}\sigma_\mathrm{C}}{\mathrm{d}\Omega}\sin\theta\,\mathrm{d}\theta\,\mathrm{d}\phi. \tag{5.5}$$

The pair production (PP) occurs for X-rays with energies > 1.02 MeV ($2 \cdot 0.51 = 1.02$, twice the rest mast energy of electron, or electron and positron), then it becomes the dominant mode of interaction between X-rays and matter. For the sake of conservation of momentum the PP occurs only near the nucleus, as a result portion of the momentum is transferred to the nucleus as recoil when the pair is created [101].

To calculate the cross-section of the incident we use the Maximon equation [102]

$$\sigma_{PP} = \frac{2\pi}{3} r_e^2 \alpha Z^2 \left(\frac{k-2}{k}\right)^3 \left(1 + \frac{1}{2}\rho + \frac{23}{40}\rho^2 + \frac{11}{60}\rho^3 + \frac{29}{960}\rho^4\right), \tag{5.6}$$

where

$$\rho = \frac{2k-4}{2+k+2\sqrt{2k}}.$$

The total photon absorption cross-section is given as the sum of the three contributions expressed by equations 5.2, 5.5, and 5.6

$$\sigma = \sigma_{PE} + \sigma_C + \sigma_{PP}. \tag{5.7}$$

The contributions along with the total absorption cross-section are plotted in Figure 5.2.
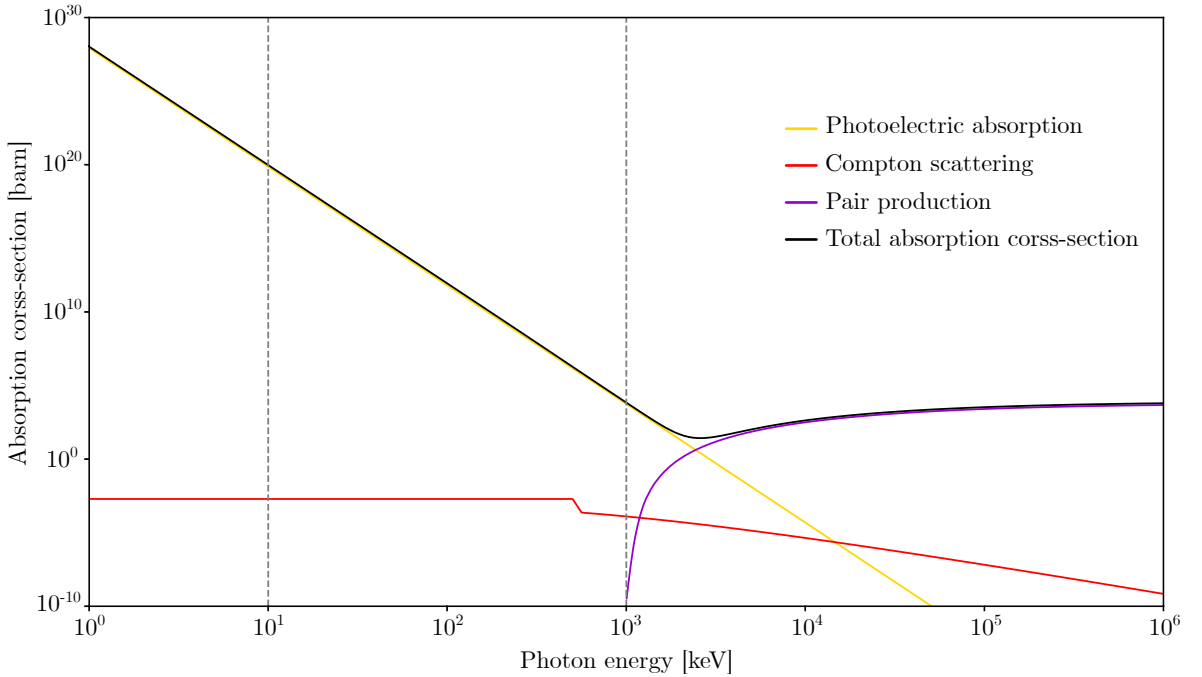
Figure 5.2: We see on this CsPbBr$_3$ LHP that the photoelectric absorption dominates for lower energies but decreases as energy increases, the pair production becomes a relevant contribution once the necessary energy limit of $2 \cdot 0.511$ MeV is reached, and the Compton scattering is present as background. The area between the two dashed lines is the energy interval used in the calculation of the linear attenuation coefficient and we see that the dominant contribution is the photoelectric absorption. (1 barn = 10^{-28} m^{-2}).

The linear attenuation coefficient is calculated for the photon absorption cross-section as

$$\mu = n \cdot \sigma = \frac{N_A \rho_M}{M} \sigma, \tag{5.8}$$

where N_A is the Avogadro's constant, ρ_M is the mass density, and M is the molar mass. The linear attenuation coefficient is calculated for a set of LMHPs CsPbBr$_{3-x}$I$_x$ ($x = 0, 0.1, 0.5, 1$) in the energy interval of $(10^1$–$10^3)$ keV, it is shown in Figure 5.3.
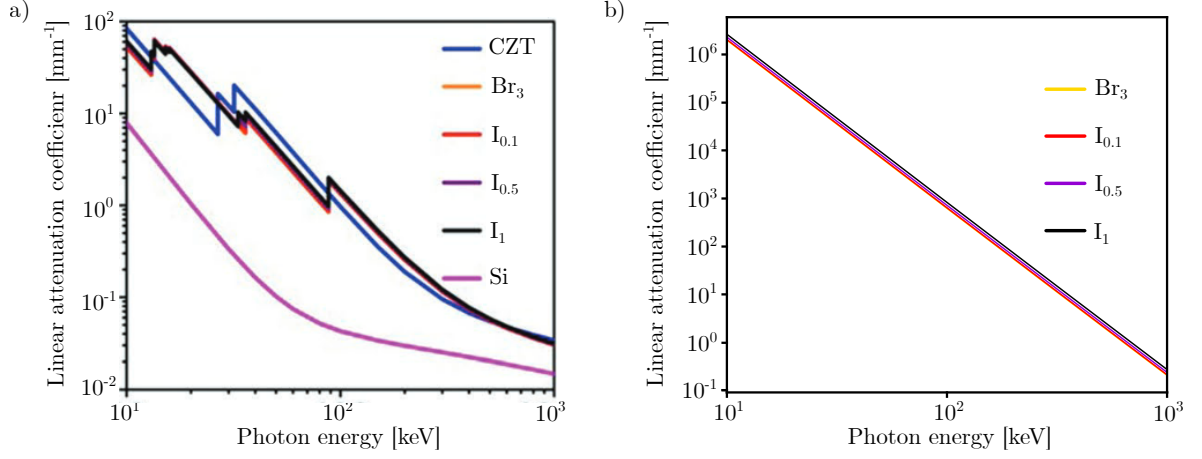
Figure 5.3: a) Linear absorption coefficient against energy for two common semiconductor materials used in ionizing radiation detectors compared to LMHPs $CsPbBr_{3-x}I_x$ ($x = 0, 0.1, 0.5, 1$), showing the LMHPs to be on par with CZT and outperform Si. Image adapted from [42]. b) Theoretical calculation of the linear attenuation coefficient (equation 5.8) for LMHPs $CsPbBr_{3-x}I_x$ ($x = 0, 0.1, 0.5, 1$).

It is important to note that we are attempting to calculate this quantity using highly approximated theory, thus we see the result values of the linear attenuation coefficient lie four orders of magnitude higher compared to the experimental data from [42]. Acquiring results closer to physical reality would require further research and employment of more complex ab initio theory.

Conclusion

Throughout this thesis, I have presented a method for construction of potential energy surfaces (PES) via the consecutive runs of activation relaxation technique noveau (ARTn). Further, I have employed classical theory to calculate the linear attenuation coefficient for selected lead mixed-halide perovskites (LMHPs).

I used the code, called CAMUS, which I helped to develop during my ERASMUS stay at the IRB Zagreb, to construct an improved PES. To start, the initial data set was generated by running an molecular dynamics calculation of two hundred 2 fs steps, starting at 400 K with continuous increase in the kinetic energy, using the Verlet algorithm. Next I extended the initial set by 200 vacancy structures, by randomly selecting structures and removing a Cs and either Br, or I atoms. This was done to include the effects of vacancies into the training model. Then I employed the ACSF descriptors to cluster the the data set including the vacancies. The created sub set of cluster centers was used further.

The main part of the CAMUS code is the so-called Sisyphus algorithm. This algorithm creates chains of ARTn runs, which look for the saddle points in the PES. The algorithm searches for connected ARTns until it reaches a given energy threshold. The connected Sisyphus path is then considered a potential transition point and the structures belonging to its points are further investigated. For purposes of efficiency the large data set of new structures was again clustered. The chosen structures were recalculated with DFT and I performed energy evaluation based on the energy difference between the DFT and CAMUS result. During the first iteration all structures recalculated with DFT were included in the retraining set, to fix some of the initial disconnect in the PES, which resulted in nonphysical structures from CAMUS. In the second iteration, structures with energy difference over 2 eV were included.

I performed two whole iterations of the CAMUS process, which resulted in 25% and 26% improvement in RMSE and MAE for energy, respectively. The improvement of these errors for forces are much greater at 42% and 32% for RMSE and MAE, respectively. This result shows that the presented method, entitled CAMUS, which I used and helped develop, is capable of expanding a suitably chosen set of data points around the PES into a much more well defined PES. If the scope of this thesis would allow, several more iterations would be performed and we would arrive at a machine-learned interatomic potential (MLIP), which would describe the complex system of $CsPbBr_{3-x}I_x$ well (determined by the use of extensive test data set). This resulting MLIP would then permit us to conduct Monte Carlo simulations to model the process of halide segregation in the LMHPs and consequently we could search for stable compositions, which we could further research as potential applicants for use in high-energy radiation detection devices.

Considering the scope of the thesis, I opted for classical theory to calculate the linear attenuation coefficient for the selected LHMPs. Those were selected according to

the paper by Zhang et al. for easier comparison with the experimental data presented by the authors. I calculated the photoelectric effect (PE), Compton scattering (CS), and pair production (PP) contributions to the absorption cross-section using the simplified Bethe-Heitler, Klein-Nishina, and Maximon equation, respectively. I plotted the calculated contributions and their sum for $CsPbBr_3$ in the interval of energies $(1$–$10^6)$ keV. The resulting curves adhere to the assumptions of the classical theory. The PE contribution is the dominant one at lower energies (below $\sim 10^3$ keV), while PP begins at the energy threshold of $(2 \cdot 511$ keV$)$ and quickly becomes the dominant contribution as PE becomes negligible. The CS, meanwhile, is present throughout in the form of background.

Furthermore, I calculated and plotted the linear attenuation coefficient for the $CsPbBr_{3-x}I_x$ $(x = 0, 0.1, 0.5, 1)$ LMHPs. Compared to the paper the calculated coefficients are four orders of magnitude larger, this is most likely due to the level of approximation of classical theory. While I was unable to match the quantitative results of experiments, what the classical theory allowed me to do, was qualitatively analyse the processes occurring when hard X-rays interact with LMHPs. To achieve high-fidelity results, comparable with experiment, would require thorough research and use of advanced ab initio methods, which proves to be non-trivial for material such as LMHP as at the core of the problem lies the calculation of dielectric function, for which even DFT is insufficient.

"I leave Sisyphus at the foot of the mountain. One always finds one's burden again. But Sisyphus teaches the higher fidelity that negates the gods and raises rocks. he too concludes that all is well. This universe henceforth without a master seems to him neither sterile nor futile. Each atom of that stone, each mineral flake of that night-filled mountain, in itself, forms a world. The struggle itself toward the heights is enough to fill a man's heart. One must imagine Sisyphus happy." [1]

References

1. CAMUS, A.; O'BRIEN, J. *The Myth of Sisyphus*. Penguin Modern Classics. London, England: Penguin Classics, 2013. ISBN 9780141182001.

2. KOJIMA, A.; TESHIMA, K.; SHIRAI, Y.; MIYASAKA, T. Organometal Halide Perovskites as Visible-Light Sensitizers for Photovoltaic Cells. *Journal of the American Chemical Society*. 2009-05-06, **131**(17), 6050–6051. ISSN 0002-7863. Available from DOI: `10.1021/ja809598r`. Publisher: American Chemical Society.

3. MANSER, J. S.; SAIDAMINOV, M. I.; CHRISTIANS, J. A.; BAKR, O. M.; KAMAT, P. V. Making and Breaking of Lead Halide Perovskites. *Accounts of Chemical Research*. 2016, **49**(2), 330–338. ISSN 0001-4842. Available from DOI: `10.1021/acs.accounts.5b00455`.

4. SHIKOH, A. S.; POLYAKOV, A. A Quantitative Analysis of the Research Trends in Perovskite Solar Cells in 2009–2019. *Physica status solidi (a)*. 2020, **217**(23). ISSN 1862-6300. Available from DOI: `10.1002/pssa.202000441`.

5. KIM, H.-S.; LEE, C.-R.; IM, J.-H.; LEE, K.-B.; MOEHL, T., et al. Lead Iodide Perovskite Sensitized All-Solid-State Submicron Thin Film Mesoscopic Solar Cell with Efficiency Exceeding 9%. *Scientific Reports*. 2012-08-21, **2**(1), 591. ISSN 2045-2322. Available from DOI: `10.1038/srep00591`. Number: 1 Publisher: Nature Publishing Group.

6. JEON, N. J.; NOH, J. H.; KIM, Y. C.; YANG, W. S.; RYU, S., et al. Solvent engineering for high-performance inorganic–organic hybrid perovskite solar cells. *Nature Materials*. 2014-09, **13**(9), 897–903. ISSN 1476-4660. Available from DOI: `10.1038/nmat4014`. Number: 9 Publisher: Nature Publishing Group.

7. JEON, N. J.; NOH, J. H.; YANG, W. S.; KIM, Y. C.; RYU, S., et al. Compositional engineering of perovskite materials for high-performance solar cells. *Nature*. 2015-01, **517**(7535), 476–480. ISSN 1476-4687. Available from DOI: `10.1038/nature14133`. Number: 7535 Publisher: Nature Publishing Group.

8. WRIGHT, A. D.; VERDI, C.; MILOT, R. L.; EPERON, G. E.; PÉREZ-OSORIO, M. A., et al. Electron–phonon coupling in hybrid lead halide perovskites. *Nature Communications*. 2016-05-26, **7**(1), 11755. ISSN 2041-1723. Available from DOI: `10.1038/ncomms11755`. Number: 1 Publisher: Nature Publishing Group.

9. AKKERMAN, Q. A.; RAINÒ, G.; KOVALENKO, M. V.; MANNA, L. Genesis, challenges and opportunities for colloidal lead halide perovskite nanocrystals. *Nature Materials*. 2018-05, **17**(5), 394–405. ISSN 1476-4660. Available from DOI: `10.1038/s41563-018-0018-4`. Number: 5 Publisher: Nature Publishing Group.

10. DU, X.; LI, J.; NIU, G.; YUAN, J.-H.; XUE, K.-H., et al. Lead halide perovskite for efficient optoacoustic conversion and application toward high-resolution ultrasound imaging. *Nature Communications*. 2021-06-07, **12**(1), 3348. ISSN 2041-1723. Available from DOI: `10.1038/s41467-021-23788-4`. Number: 1 Publisher: Nature Publishing Group.

11. PRASANNA, R.; LEIJTENS, T.; DUNFIELD, S. P.; RAIFORD, J. A.; WOLF, E. J., et al. Design of low bandgap tin–lead halide perovskite solar cells to achieve thermal, atmospheric and operational stability. *Nature Energy*. 2019-11, **4**(11), 939–947. ISSN 2058-7546. Available from DOI: `10.1038/s41560-019-0471-6`. Number: 11 Publisher: Nature Publishing Group.

12. WANG, H.; BIAN, H.; JIN, Z.; ZHANG, H.; LIANG, L., et al. Cesium Lead Mixed-Halide Perovskites for Low-Energy Loss Solar Cells with Efficiency Beyond 17%. *Chemistry of Materials*. 2019, **31**(16), 6231–6238. ISSN 0897-4756. Available from DOI: `10.1021/acs.chemmater.9b02248`.

13. BROWN, A. A. M.; DAMODARAN, B.; JIANG, L.; TEY, J. N.; PU, S. H., et al. Lead Halide Perovskite Nanocrystals: Room Temperature Syntheses toward Commercial Viability. *Advanced Energy Materials*. 2020, **10**(34). ISSN 1614-6832. Available from DOI: `10.1002/aenm.202001349`.

14. MCMEEKIN, D. P.; SADOUGHI, G.; REHMAN, W.; EPERON, G. E.; SALIBA, M., et al. A mixed-cation lead mixed-halide perovskite absorber for tandem solar cells. *Science*. 2016, **351**(6269), 151–155. ISSN 0036-8075. Available from DOI: `10.1126/science.aad5845`.

15. DESCHLER, F.; PRICE, M.; PATHAK, S.; KLINTBERG, L. E.; JARAUSCH, D.-D., et al. High Photoluminescence Efficiency and Optically Pumped Lasing in Solution-Processed Mixed Halide Perovskite Semiconductors. *The Journal of Physical Chemistry Letters*. 2014, **5**(8), 1421–1426. ISSN 1948-7185. Available from DOI: `10.1021/jz5005285`.

16. YAKUNIN, S.; DIRIN, D. N.; SHYNKARENKO, Y.; MORAD, V.; CHERNIUKH, I., et al. Detection of gamma photons using solution-grown single crystals of hybrid lead halide perovskites. *Nature Photonics*. 2016, **10**(9), 585–589. ISSN 1749-4885. Available from DOI: `10.1038/nphoton.2016.139`.

17. VIGHNESH, K.; WANG, S.; LIU, H.; ROGACH, A. L. Hot-Injection Synthesis Protocol for Green-Emitting Cesium Lead Bromide Perovskite Nanocrystals. *ACS Nano*. 2022-12-27, **16**(12), 19618–19625. ISSN 1936-0851. Available from DOI: `10.1021/acsnano.2c11689`. Publisher: American Chemical Society.

18. DUTTA, A.; BEHERA, R. K.; DUTTA, S. K.; DAS ADHIKARI, S.; PRADHAN, N. Annealing CsPbX3 (X = Cl and Br) Perovskite Nanocrystals at High Reaction Temperatures: Phase Change and Its Prevention. *The Journal of Physical Chemistry Letters*. 2018-11-15, **9**(22), 6599–6604. Available from DOI: `10.1021/acs.jpclett.8b02825`. Publisher: American Chemical Society.

19. YOON, S. J.; STAMPLECOSKIE, K. G.; KAMAT, P. V. How Lead Halide Complex Chemistry Dictates the Composition of Mixed Halide Perovskites. *The Journal of Physical Chemistry Letters*. 2016-04-07, **7**(7), 1368–1373. Available from DOI: `10.1021/acs.jpclett.6b00433`. Publisher: American Chemical Society.

20. BRENNAN, M. C.; RUTH, A.; KAMAT, P. V.; KUNO, M. Photoinduced Anion Segregation in Mixed Halide Perovskites. *Trends in Chemistry*. 2020-04-01, **2**(4), 282–301. ISSN 2589-7209, ISSN 2589-5974. Available from DOI: `10.1016/j.trechm.2020.01.010`. Publisher: Elsevier.

21. NEDELCU, G.; PROTESESCU, L.; YAKUNIN, S.; BODNARCHUK, M. I.; GROTEVENT, M. J., et al. Fast Anion-Exchange in Highly Luminescent Nanocrystals of Cesium Lead Halide Perovskites (CsPbX3, X = Cl, Br, I). *Nano Letters*. 2015-08-12, **15**(8), 5635–5640. ISSN 1530-6984. Available from DOI: `10.1021/acs.nanolett.5b02404`. Publisher: American Chemical Society.

22. WEI, H.; HUANG, J. Halide lead perovskites for ionizing radiation detection. *Nature Communications*. 2019-03-06, **10**(1), 1066. ISSN 2041-1723. Available from DOI: `10.1038/s41467-019-08981-w`. Number: 1 Publisher: Nature Publishing Group.

23. STOUMPOS, C. C.; MALLIAKAS, C. D.; PETERS, J. A.; LIU, Z.; SEBASTIAN, M., et al. Crystal Growth of the Perovskite Semiconductor CsPbBr3: A New Material for High-Energy Radiation Detection. *Crystal Growth & Design*. 2013-07-03, **13**(7), 2722–2727. ISSN 1528-7483. Available from DOI: `10.1021/cg400645t`. Publisher: American Chemical Society.

24. GAO, L.; YAN, Q. Recent Advances in Lead Halide Perovskites for Radiation Detectors. *Solar RRL*. 2020, **4**(2), 1900210. ISSN 2367-198X. Available from DOI: `10.1002/solr.201900210`.

25. KAKAVELAKIS, G.; GEDDA, M.; PANAGIOTOPOULOS, A.; KYMAKIS, E.; ANTHOPOULOS, T. D., et al. Metal Halide Perovskites for High-Energy Radiation Detection. *Advanced Science*. 2020, **7**(22), 2002098. ISSN 2198-3844. Available from DOI: `10.1002/advs.202002098`.

26. GUERRA, M.; MANSO, M.; LONGELIN, S.; PESSANHA, S.; CARVALHO, M. L. Performance of three different Si X-ray detectors for portable XRF spectrometers in cultural heritage applications. *Journal of Instrumentation*. 2012-10, **7**(10), C10004. ISSN 1748-0221. Available from DOI: `10.1088/1748-0221/7/10/C10004`.

27. ARFELLI, F.; BARBIELLINI, G.; CANTATORE, G.; CASTELLI, E.; CRISTAUDO, P., et al. Silicon X-ray detector for synchrotron radiation digital radiology. *Nuclear Instruments and Methods in Physics Research Section A: Accelerators, Spectrometers, Detectors and Associated Equipment*. 1994-12-30, **353**(1), 366–370. ISSN 0168-9002. Available from DOI: `10.1016/0168-9002(94)91677-2`.

28. KASAP, S.; FREY, J. B.; BELEV, G.; TOUSIGNANT, O.; MANI, H., et al. Amorphous and polycrystalline photoconductors for direct conversion flat panel x-ray image sensors. *Sensors (Basel, Switzerland)*. 2011, **11**(5), 5112–5157. ISSN 1424-8220. Available from DOI: `10.3390/s110505112`.

29. NAGARKAR, V.; GUPTA, T.; MILLER, S.; KLUGERMAN, Y.; SQUILLANTE, M., et al. Structured CsI(Tl) scintillators for X-ray imaging applications. *IEEE Transactions on Nuclear Science*. 1998-06, **45**(3), 492–496. ISSN 1558-1578. Available from DOI: `10.1109/23.682433`. Conference Name: IEEE Transactions on Nuclear Science.

30. STARKENBURG, D. J.; JOHNS, P. M.; BACIAK, J. E.; NINO, J. C.; XUE, J. Thin film organic photodetectors for indirect X-ray detection demonstrating low dose rate sensitivity at low voltage operation. *Journal of Applied Physics*. 2017-12-12, **122**(22), 225502. ISSN 0021-8979. Available from DOI: `10.1063/1.4999759`.

31. KULBAK, M.; GUPTA, S.; KEDEM, N.; LEVINE, I.; BENDIKOV, T., et al. Cesium Enhances Long-Term Stability of Lead Bromide Perovskite-Based Solar Cells. *The Journal of Physical Chemistry Letters*. 2016-01-07, **7**(1), 167–172. Available from DOI: `10.1021/acs.jpclett.5b02597`. Publisher: American Chemical Society.

32. RIKNER, G.; GRUSELL, E. Effects of radiation damage on p-type silicon detectors. *Physics in Medicine & Biology*. 1983-11, **28**(11), 1261. ISSN 0031-9155. Available from DOI: `10.1088/0031-9155/28/11/006`.

33. HUNTER, D. M.; BELEV, G.; KASAP, S.; YAFFE, M. J. Measured and calculated K-fluorescence effects on the MTF of an amorphous-selenium based CCD x-ray detector. *Medical Physics*. 2012-02, **39**(2), 608–622. ISSN 0094-2405. Available from DOI: `10.1118/1.3673957`.

34. ZENTAI, G.; PARTAIN, L. D.; PAVLYUCHKOVA, R.; PROANO, C.; VIRSHUP, G. F., et al. Mercuric iodide and lead iodide x-ray detectors for radiographic and fluoroscopic medical imaging. In: *Medical Imaging 2003: Physics of Medical Imaging*. SPIE, 2003-06-05, vol. 5030, pp. 77–91. Available from DOI: `10.1117/12.480227`.

35. IVANOV, Y. M.; KANEVSKY, V. M.; DVORYANKIN, V. F.; ARTEMOV, V. V.; POLYAKOV, A. N., et al. The possibilities of using semi-insulating CdTe crystals as detecting material for X-ray imaging radiography. *physica status solidi (c)*. 2003, **n/a**(3), 840–844. ISSN 1610-1642. Available from DOI: `10.1002/pssc.200306258`.

36. BELLAZZINI, R.; SPANDRE, G.; BREZ, A.; MINUTI, M.; PINCHERA, M., et al. Chromatic X-ray imaging with a fine pitch CdTe sensor coupled to a large area photon counting pixel ASIC. *Journal of Instrumentation*. 2013-02, **8**(2), C02028. ISSN 1748-0221. Available from DOI: `10.1088/1748-0221/8/02/C02028`.

37. KIM, Y. C.; KIM, K. H.; SON, D.-Y.; JEONG, D.-N.; SEO, J.-Y., et al. Printable organometallic perovskite enables large-area, low-dose X-ray imaging. *Nature*. 2017-10, **550**(7674), 87–91. ISSN 1476-4687. Available from DOI: `10.1038/nature24032`. Publisher: Nature Publishing Group.

38. WEI, H.; FANG, Y.; MULLIGAN, P.; CHUIRAZZI, W.; FANG, H.-H., et al. Sensitive X-ray detectors made of methylammonium lead tribromide perovskite single crystals. *Nature Photonics*. 2016-05, **10**(5), 333–339. ISSN 1749-4893. Available from DOI: `10.1038/nphoton.2016.41`. Number: 5 Publisher: Nature Publishing Group.

39. WEI, W.; ZHANG, Y.; XU, Q.; WEI, H.; FANG, Y., et al. Monolithic integration of hybrid perovskite single crystals with heterogenous substrate for highly sensitive X-ray imaging. *Nature Photonics*. 2017-05, **11**(5), 315–321. ISSN 1749-4893. Available from DOI: `10.1038/nphoton.2017.43`. Publisher: Nature Publishing Group.

40. PAN, W.; YANG, B.; NIU, G.; XUE, K.-H.; DU, X., et al. Hot-Pressed CsPbBr3 Quasi-Monocrystalline Film for Sensitive Direct X-ray Detection. *Advanced Materials*. 2019, **31**(44), 1904405. ISSN 1521-4095. Available from DOI: `10.1002/adma.201904405`.

41. HEO, J. H.; SHIN, D. H.; PARK, J. K.; KIM, D. H.; LEE, S. J., et al. High-Performance Next-Generation Perovskite Nanocrystal Scintillator for Nondestructive X-Ray Imaging. *Advanced Materials*. 2018, **30**(40), 1801743. ISSN 1521-4095. Available from DOI: `10.1002/adma.201801743`.

42. ZHANG, P.; HUA, Y.; XU, Y.; SUN, Q.; LI, X., et al. Ultrasensitive and Robust 120 keV Hard X-Ray Imaging Detector based on Mixed-Halide Perovskite CsPbBr(3-n)I(n) Single Crystals. *Advanced Materials*. 2022, **34**(12), 2106562. ISSN 1521-4095. Available from DOI: `10.1002/adma.202106562`.

43. JIANG, H.; CUI, S.; CHEN, Y.; ZHONG, H. Ion exchange for halide perovskite: From nanocrystal to bulk materials. *Nano Select*. 2021, **2**(11), 2040–2060. ISSN 2688-4011. Available from DOI: `10.1002/nano.202100084`.

44. AKKERMAN, Q. A.; D'INNOCENZO, V.; ACCORNERO, S.; SCARPELLINI, A.; PETROZZA, A., et al. Tuning the Optical Properties of Cesium Lead Halide Perovskite Nanocrystals by Anion Exchange Reactions. *Journal of the American Chemical Society*. 2015-08-19, **137**(32), 10276–10281. ISSN 0002-7863. Available from DOI: `10.1021/jacs.5b05602`. Publisher: American Chemical Society.

45. KOVALENKO, M. V.; PROTESESCU, L.; BODNARCHUK, M. I. Properties and potential optoelectronic applications of lead halide perovskite nanocrystals. *Science*. 2017, **358**(6364), 745–750. ISSN 0036-8075. Available from DOI: `10.1126/science.aam7093`.

46. LYU, R.; CUI, Z.; ELGIN, J.; CO, A. C.; WU, Y. Photoelectrochemistry of Methylviologen Lead Iodide: Achieving Stability inside a Polar Solvent. *The Journal of Physical Chemistry C*. 2023-08-17, **127**(32), 15852–15860. ISSN 1932-7447. Available from DOI: `10.1021/acs.jpcc.3c04054`. Publisher: American Chemical Society.

47. ZHENG, Y.; YANG, S. Stabilization Techniques of Lead Halide Perovskite for Photovoltaic Applications. *Solar RRL*. 2022, **6**(1), 2100710. ISSN 2367-198X. Available from DOI: `10.1002/solr.202100710`.

48. DE GIORGI, M. L.; MILANESE, S.; KLINI, A.; ANNI, M. Environment-Induced Reversible Modulation of Optical and Electronic Properties of Lead Halide Perovskites and Possible Applications to Sensor Development: A Review. *Molecules*. 2021-01, **26**(3), 705. ISSN 1420-3049. Available from DOI: `10.3390/molecules26030705`. Number: 3 Publisher: Multidisciplinary Digital Publishing Institute.

49. PAN, Z.; WU, L.; JIANG, J.; SHEN, L.; YAO, K. Searching for High-Quality Halide Perovskite Single Crystals toward X-ray Detection. *The Journal of Physical Chemistry Letters*. 2022-04-07, **13**(13), 2851–2861. Available from DOI: `10.1021/acs.jpclett.2c00450`. Publisher: American Chemical Society.

50. ZHANG, Q.; WANG, B.; ZHENG, W.; KONG, L.; WAN, Q., et al. Ceramic-like stable CsPbBr3 nanocrystals encapsulated in silica derived from molecular sieve templates. *Nature Communications*. 2020-01-07, **11**(1), 31. ISSN 2041-1723. Available from DOI: 10.1038/s41467-019-13881-0. Number: 1 Publisher: Nature Publishing Group.

51. WANG, Y.; QUINTANA, X.; KIM, J.; GUAN, X.; HU, L., et al. Phase segregation in inorganic mixed-halide perovskites: from phenomena to mechanisms. *Photonics Research*. 2020-11-01, **8**(11), A56–A71. ISSN 2327-9125. Available from DOI: 10.1364/PRJ.402411. Publisher: Optica Publishing Group.

52. FROST, J. M.; WALSH, A. What Is Moving in Hybrid Halide Perovskite Solar Cells? *Accounts of Chemical Research*. 2016-03-15, **49**(3), 528–535. ISSN 0001-4842. Available from DOI: 10.1021/acs.accounts.5b00431. Publisher: American Chemical Society.

53. SU, Y.; MA, W.; YANG, Y. M. Perovskite semiconductors for direct X-ray detection and imaging. *Journal of Semiconductors*. 2020-05, **41**(5), 051204. ISSN 1674-4926. Available from DOI: 10.1088/1674-4926/41/5/051204. Publisher: Chinese Institute of Electronics.

54. REIMER, L. *Scanning Electron Microscopy*. Second Edition. Berlin, Heidelberg: Springer Berlin Heidelberg, 1998. ISBN 978-3-642-08372-3. Available from DOI: 10.1007/978-3-540-38967-5.

55. REIMER, L.; KOHL, H. *Transmission Electron Microscopy*. Fifth edition. New York, NY: Springer New York, 2008. ISBN 978-0-387-40093-8. Available from DOI: 10.1007/978-0-387-40093-8.

56. JAANISO, R. *Semiconductor Gas Sensors*. Second Edition. Elsevier, 2020. ISBN 9780081025598. Available from DOI: 10.1016/C2017-0-00001-0.

57. *ADVACAM Photon Counting Detector Technology Manufacturer* [Advacam] [online]. [visited on 2024-04-28]. Available from: <https://advacam.com/technology/>.

58. *Stanford: Advanced Optical Ceramics Laboratory* [online]. [visited on 2024-04-28]. Available from: <https://web.stanford.edu/group/scintillators/scintillators.html>.

59. PARR, R. G.; WEITAO, Y. *Density-Functional Theory of Atoms and Molecules*. Oxford University Press, 1995. ISBN 9780195092769. Available from DOI: 10.1093/oso/9780195092769.001.0001.

60. BAGAYOKO, D. Understanding density functional theory (DFT) and completing it in practice. *AIP Advances*. 2014, **4**(12). ISSN 2158-3226. Available from DOI: 10.1063/1.4903408.

61. WIDAYANI; WUNGU, T. D. K.; MARSHA, S. E.; SUPRIJADI. Study of Target Recognition of MAA-based Molecularly Imprinted Polymer (MIP) Using Density Functional Theory (DFT) Computation on the Interaction of Methacrylic Acid (MAA)-D-Glucose. *Journal of Polymer and Biopolymer Physics Chemistry*. 2017-09-29, **5**(1), 10–12. Available from DOI: 10.12691/jpbpc-5-1-2. Number: 1 Publisher: Science and Education Publishing.

62. LEJAEGHERE, K.; BIHLMAYER, G.; BJÖRKMAN, T.; BLAHA, P.; BLÜGEL, S., et al. Reproducibility in density functional theory calculations of solids. *Science*. 2016-03-25, **351**(6280), aad3000. Available from DOI: `10.1126/science.aad3000`. Publisher: American Association for the Advancement of Science.

63. JONES, R. O. Density functional theory: Its origins, rise to prominence, and future. *Reviews of Modern Physics*. 2015-08-25, **87**(3), 897–923. Available from DOI: `10.1103/RevModPhys.87.897`. Publisher: American Physical Society.

64. MUSAELIAN, A.; BATZNER, S.; JOHANSSON, A.; SUN, L.; OWEN, C. J., et al. Learning local equivariant representations for large-scale atomistic dynamics. *Nature Communications*. 2023-02-03, **14**(1), 579. ISSN 2041-1723. Available from DOI: `10.1038/s41467-023-36329-y`. Number: 1 Publisher: Nature Publishing Group.

65. ALDER, B. J.; WAINWRIGHT, T. E. Phase Transition for a Hard Sphere System. *The Journal of Chemical Physics*. 2004-08-13, **27**(5), 1208–1209. ISSN 0021-9606. Available from DOI: `10.1063/1.1743957`.

66. VERLET, L. Computer "Experiments" on Classical Fluids. I. Thermodynamical Properties of Lennard-Jones Molecules. *Physical Review*. 1967-07-05, **159**(1), 98–103. Available from DOI: `10.1103/PhysRev.159.98`. Publisher: American Physical Society.

67. MELLER, J. Molecular Dynamics. In: *Encyclopedia of Life Sciences*. John Wiley & Sons, Ltd, 2001. ISBN 978-0-470-01590-2. Available from DOI: `10.1038/npg.els.0003048`.

68. HOLLINGSWORTH, S. A.; DROR, R. O. Molecular Dynamics Simulation for All. *Neuron*. 2018-09-19, **99**(6), 1129–1143. ISSN 0896-6273. Available from DOI: `10.1016/j.neuron.2018.08.011`.

69. KARPLUS, M.; MCCAMMON, J. A. Molecular dynamics simulations of biomolecules. *Nature Structural Biology*. 2002-09, **9**(9), 646–652. ISSN 1072-8368. Available from DOI: `10.1038/nsb0902-646`.

70. SALOMON-FERRER, R.; GÖTZ, A. W.; POOLE, D.; LE GRAND, S.; WALKER, R. C. Routine Microsecond Molecular Dynamics Simulations with AMBER on GPUs. 2. Explicit Solvent Particle Mesh Ewald. *Journal of Chemical Theory and Computation*. 2013-09-10, **9**(9), 3878–3888. ISSN 1549-9618. Available from DOI: `10.1021/ct400314y`. Publisher: American Chemical Society.

71. STONE, J. E.; HALLOCK, M. J.; PHILLIPS, J. C.; PETERSON, J. R.; LUTHEY-SCHULTEN, Z., et al. Evaluation of Emerging Energy-Efficient Heterogeneous Computing Platforms for Biomolecular and Cellular Simulation Workloads. In: *2016 IEEE International Parallel and Distributed Processing Symposium Workshops (IPDPSW)*. 2016-05, pp. 89–100. Available from DOI: `10.1109/IPDPSW.2016.130`.

72. LARSSON, P.; HESS, B.; LINDAHL, E. Algorithm improvements for molecular dynamics simulations. *WIREs Computational Molecular Science*. 2011, **1**(1), 93–108. ISSN 1759-0884. Available from DOI: `10.1002/wcms.3`.

73. CHEN, K.; ZENG, K. Performance Optimization Model of Molecular Dynamics Simulation Based on Machine Learning and Data Mining Algorithm. *Mobile Information Systems*. 2022-09-10, **2022**, e4553446. ISSN 1574-017X. Available from DOI: `10.1155/2022/4553446`. Publisher: Hindawi.

74. THOMPSON, A. P.; AKTULGA, H. M.; BERGER, R.; BOLINTINEANU, D. S.; BROWN, W. M., et al. LAMMPS - a flexible simulation tool for particle-based materials modeling at the atomic, meso, and continuum scales. *Computer Physics Communications*. 2022-02-01, **271**, 108171. ISSN 0010-4655. Available from DOI: `10.1016/j.cpc.2021.108171`.

75. DIAS, C. S. *Molecular Dynamics Simulations of Active Matter using LAMMPS*. arXiv, 2021-02-24. No. arXiv:2102.10399. Available from DOI: `10.48550/arXiv.2102.10399`.

76. PLIMPTON, S. Fast Parallel Algorithms for Short-Range Molecular Dynamics. *Journal of Computational Physics*. 1995-03-01, **117**(1), 1–19. ISSN 0021-9991. Available from DOI: `10.1006/jcph.1995.1039`.

77. GUÉNOLÉ, J.; NÖHRING, W. G.; VAID, A.; HOULLÉ, F.; XIE, Z., et al. Assessment and optimization of the fast inertial relaxation engine (fire) for energy minimization in atomistic simulations and its implementation in lammps. *Computational Materials Science*. 2020-04-01, **175**, 109584. ISSN 0927-0256. Available from DOI: `10.1016/j.commatsci.2020.109584`.

78. BITZEK, E.; KOSKINEN, P.; GÄHLER, F.; MOSELER, M.; GUMBSCH, P. Structural Relaxation Made Simple. *Physical Review Letters*. 2006-10-27, **97**(17), 170201. Available from DOI: `10.1103/PhysRevLett.97.170201`. Publisher: American Physical Society.

79. EIDEL, B.; STUKOWSKI, A.; SCHRÖDER, J. Energy-Minimization in Atomic-to-Continuum Scale-Bridging Methods. *PAMM*. 2011, **11**(1), 509–510. ISSN 1617-7061. Available from DOI: `10.1002/pamm.201110246`.

80. JAY, A.; GUNDE, M.; SALLES, N.; POBERŽNIK, M.; MARTIN-SAMOS, L., et al. Activation–Relaxation Technique: An efficient way to find minima and saddle points of potential energy surfaces. *Computational Materials Science*. 2022-06-15, **209**, 111363. ISSN 0927-0256. Available from DOI: `10.1016/j.commatsci.2022.111363`.

81. LANCZOS, C. An iteration method for the solution of the eigenvalue problem of linear differential and integral operators. *Journal of Research of the National Bureau of Standards*. 1950-10, **45**(4), 255. ISSN 0091-6635. Available from DOI: `10.6028/jres.045.026`.

82. FLANAGAN, F. J.; KAZDAN, J. L. *Calculus Two: Linear and Nonlinear Functions*. Second Edition. Springer, 1990. ISBN 978-0387973883.

83. POBERŽNIK, M.; GUNDE, M.; SALLES, N.; JAY, A.; HEMERYCK, A., et al. *Partn: A Plugin Implementation of the Activation Relaxation Technique Nouveau Hijacking a Minimisation Algorithm*. Rochester, NY, 2023-02-16. No. 4360939. Available from DOI: `10.2139/ssrn.4360939`.

84. FRIEDERICH, P.; HÄSE, F.; PROPPE, J.; ASPURU-GUZIK, A. Machine-learned potentials for next-generation matter simulations. *Nature Materials*. 2021-06, **20**(6), 750–761. ISSN 1476-4660. Available from DOI: `10.1038/s41563-020-0777-6`. Number: 6 Publisher: Nature Publishing Group.

85. BEHLER, J.; PARRINELLO, M. Generalized Neural-Network Representation of High-Dimensional Potential-Energy Surfaces. *Physical Review Letters*. 2007-04-02, **98**(14), 146401. Available from DOI: `10.1103/PhysRevLett.98.146401`. Publisher: American Physical Society.

86. BEHLER, J. Neural network potential-energy surfaces in chemistry: a tool for large-scale simulations. *Physical Chemistry Chemical Physics*. 2011-10-04, **13**(40), 17930–17955. ISSN 1463-9084. Available from DOI: `10.1039/C1CP21668F`. Publisher: The Royal Society of Chemistry.

87. FU, X.; WU, Z.; WANG, W.; XIE, T.; KETEN, S., et al. *Forces are not Enough: Benchmark and Critical Evaluation for Machine Learning Force Fields with Molecular Simulations*. arXiv, 2023-08-26. No. arXiv:2210.07237. Available from DOI: `10.48550/arXiv.2210.07237`.

88. MUSAELIAN, A.; JOHANSSON, A.; BATZNER, S.; KOZINSKY, B. *Scaling the leading accuracy of deep equivariant models to biomolecular simulations of realistic size*. arXiv, 2023-04-19. No. arXiv:2304.10061. Available from DOI: `10.48550/arXiv.2304.10061`.

89. *GitHub - ovcarj/camus: This is a working repository for the 'CAMUS' algorithm (working name also) for automatizing refinement of ML models via iterative artN searches*. [online]. [visited on 2024-05-17]. Available from: `<https://github.com/ovcarj/camus>`.

90. KRESSE, G.; HAFNER, J. Ab initio molecular dynamics for liquid metals. *Physical Review B*. 1993-01-01, **47**(1), 558–561. Available from DOI: `10.1103/PhysRevB.47.558`. Publisher: American Physical Society.

91. KRESSE, G.; FURTHMÜLLER, J. Efficiency of ab-initio total energy calculations for metals and semiconductors using a plane-wave basis set. *Computational Materials Science*. 1996-07-01, **6**(1), 15–50. ISSN 0927-0256. Available from DOI: `10.1016/0927-0256(96)00008-0`.

92. KRESSE, G.; FURTHMÜLLER, J. Efficient iterative schemes for ab initio total-energy calculations using a plane-wave basis set. *Physical Review B*. 1996-10-15, **54**(16), 11169–11186. Available from DOI: `10.1103/PhysRevB.54.11169`. Publisher: American Physical Society.

93. HIMANEN, L.; JÄGER, M. O. J.; MOROOKA, E. V.; FEDERICI CANOVA, F.; RANAWAT, Y. S., et al. DScribe: Library of descriptors for machine learning in materials science. *Computer Physics Communications*. 2020, **247**, 106949. ISSN 0010-4655. Available from DOI: `10.1016/j.cpc.2019.106949`.

94. LAAKSO, J.; HIMANEN, L.; HOMM, H.; MOROOKA, E. V.; JÄGER, M. O., et al. Updates to the DScribe library: New descriptors and derivatives. *The Journal of Chemical Physics*. 2023, **158**(23).

95. BEHLER, J. Atom-centered symmetry functions for constructing high-dimensional neural network potentials. *The Journal of Chemical Physics*. 2011-02-16, **134**(7), 074106. ISSN 0021-9606. Available from DOI: `10.1063/1.3553717`.

96. DAVISSON, C. M. *Interaction of GAMMA-RADIATION with Matter.* Vol. 1. 1965-01-01. Conference Name: Alpha-, Beta- and Gamma-ray Spectroscopy Pages: 37 ADS Bibcode: 1965abgs.conf...37D.

97. FORNALSKI, K. W. Simple empirical correction functions to cross sections of the photoelectric effect, Compton scattering, pair and triplet production for carbon radiation shields for intermediate and high photon energies. *Journal of Physics Communications.* 2018-03, **2**(3), 035038. ISSN 2399-6528. Available from DOI: `10.1088/2399-6528/aab408`. Publisher: IOP Publishing.

98. CHRISTILLIN, P. Nuclear Compton scattering. *Journal of Physics G: Nuclear Physics.* 1986-09, **12**(9), 837. ISSN 0305-4616. Available from DOI: `10.1088/0305-4616/12/9/008`.

99. KLEIN, O.; NISHINA, Y. Über die Streuung von Strahlung durch freie Elektronen nach der neuen relativistischen Quantendynamik von Dirac. *Zeitschrift für Physik.* 1929-11-01, **52**(11), 853–868. ISSN 0044-3328. Available from DOI: `10.1007/BF01366453`.

100. WEINBERG, S. *The Quantum Theory of Fields.* First Edition. Cambridge University Press, 2013. ISBN 9780521670531. Available from DOI: `10.1017/CBO9781139644167`.

101. HUBBELL, J. H.; GIMM, H. A.; O/VERBO/, I. Pair, Triplet, and Total Atomic Cross Sections (and Mass Attenuation Coefficients) for 1 MeV-100 GeV Photons in Elements Z=1 to 100. *Journal of Physical and Chemical Reference Data.* 1980-10-01, **9**(4), 1023–1148. ISSN 0047-2689. Available from DOI: `10.1063/1.555629`.

102. MAXIMON, L. C. SIMPLE ANALYTIC EXPRESSIONS FOR THE TOTAL BORN APPROXIMATION CROSS SECTION FOR PAIR PRODUCTION IN A COULOMB FIELD. *J. Res. Nat. Bur. Stand., B, 72: 79-88(Jan.-Mar. 1968).* 1968-01-01. Available from DOI: `10.6028/jres.072B.011`. Institution: National Bureau of Standards, Washington, DC (United States).

List of abbreviations

LHP	....	lead halide perovskite
LMHP	....	lead mixed-halide perovskite
OA	....	oleic acid
OLA	....	oleylamine
NC	....	nanocrystal
PES	....	potential energy surface
DFT	....	density functional theory
KSE	....	Kohn-Sham equation
SCF	....	self-consistent field
MD	....	molecular dynamics
LAMMPS	....	large-scale atomic/molecular massively parallel simulator
FIRE	....	fast inertial relaxation engine
ARTn	....	activation relaxation technique noveau
MC	....	Monte Carlo
MLIP	....	machine-learned interatomic potential
NN	....	neural network
MPNN	....	message-passing neural network
ACSF	....	atomic-centered symmetry functions
MAE	....	mean absolute error
RMSE	....	root-mean square error
PE	....	photoelectric effect
CS	....	Compton scattering
PP	....	pair production